Separation and Purification Technology 311 (2023) 123320

Contents lists available at ScienceDirect

Separation and Purification Technology

journal homepage: www.elsevier.com/locate/seppur

Heterojunction of (P, S) co-doped g-C_3N_4 and 2D TiO_2 for improved carbamazepine and acetaminophen photocatalytic degradation

Elvana Cako [a,*], Szymon Dudziak [a], Paweł Głuchowski [b], Grzegorz Trykowski [c], Marcin Pisarek [d], Agnieszka Fiszka Borzyszkowska [a], Karol Sikora [e], Anna Zielińska-Jurek [a,*]

[a] *Department of Process Engineering and Chemical Technology, Faculty of Chemistry, Gdańsk University of Technology, G. Narutowicza 11/12, 80-233 Gdańsk, Poland*
[b] *Institute of Low Temperature and Structural Research, Polish Academy of Sciences, Okólna 2, 50-422 Wrocław, Poland*
[c] *Faculty of Chemistry, Nicolaus Copernicus University, Gagarina 7, 87-100 Toruń, Poland*
[d] *Institute of Physical Chemistry, Polish Academy of Sciences, Kasprzaka 44/52, 01–224 Warsaw, Poland*
[e] *Faculty of Pharmacy, Department of Inorganic Chemistry, Medical University of Gdansk, Al. Gen. J. Hallera 107, 80-416 Gdańsk, Poland*

ARTICLE INFO

Keywords:
2D TiO_2 nanosheets
Photocatalysis
Doping
g-C_3N_4
Carbamazepine
Acetaminophen
Pharmaceutical degradation
Photooxidation process

ABSTRACT

Novel photocatalysts of phosphorus and sulfur co-doped graphitic carbon nitride incorporated in 2D TiO_2 structure were successfully fabricated and applied for solar-driven degradation of emerging pollutants from the group of pharmaceuticals not susceptible to biodegradation. The hybrid photocatalysts with different loadings of (P, S)-doped g-C_3N_4 were characterized by X-ray diffraction (XRD), Fourier transform infrared spectroscopy (FTIR), UV–vis diffuse reflectance spectroscopy (DR/UV–vis), photoluminescence (PL) spectroscopy, X-ray photoelectron spectroscopy (XPS), Raman spectroscopy, and transmission electron microscopy (TEM). The optimum (P, S)-doped g-C_3N_4/TiO_2 (5 %) composite revealed improved photocatalytic activity towards the degradation of carbamazepine and acetaminophen. For CBZ, about 100 % degradation was achieved in less than 30 min of photodegradation, whereas for ACT, the complete removal was observed in 60 min of irradiation under simulated solar light. The multi-anion doped g-C_3N_4/2D TiO_2 composite demonstrated an excellent synergy towards the degradation of CBZ and ACT with a synergy index of 1.35 and 1.62. Moreover, the mineralization efficiency measured as TOC removal was 76 % and 40 % for CBZ and ACT, respectively. The reactive oxygen species responsible for the degradation of selected pharmaceuticals are superoxide ($^{\bullet}O_2^-$) and hydroxyl radicals ($HO^{\bullet}$), and the kinetics of reactions proved to fit the first-order kinetics with a rate constant of 0.21 min^{-1} for CBZ degradation and 0.074 min^{-1} for ACT degradation. Our results suggest that (P, S)-doped g-C_3N_4/ 2D TiO_2 heterostructure is a Z-scheme heterojunction, which can effectively separate photogenerated charge carriers. The emissions and decay times analyzed for single components and the optimal (P, S)-doped g-C_3N_4/ 2D TiO_2 (5 %) composite confirmed interfacial charge transfer between TiO_2 nanosheets and (P, S)-g-C_3N_4 and more effective separation of electron-hole pairs. Identification of carbamazepine and acetaminophen intermediates was performed using LC-MS analysis in combination with additional DFT calculations of the possible by-products formation. Regarding reusability, the photocatalytic activity of (P, S)-doped g-C_3N_4/ 2D TiO_2 (5 %) was stable after subsequent cycles of carbamazepine and acetaminophen degradation.

1. Introduction

Water is a vital resource for natural ecosystems and human life. Therefore, assuring a high quality of water and protecting it from contamination is one of the critical goals of sustainable development in the contemporary world. In recent years, pharmaceutically active compounds and personal care products have become a class of emerging environmental contaminants that are extensively and increasingly being detected in aquatic systems [1–3]. Some of the commonly and worldwide used non-steroidal anti-inflammatory drugs such as ibuprofen, diclofenac, ketoprofen, naproxen and acetaminophen are not susceptible to biological degradation, therefore passing through a cycle of biological treatment in the unchanged form being detected in trace amounts in surface waters, maritime and wastewater treatment plants [4–6]. Among them, acetaminophen (ACT), also commonly known as paracetamol, is a pharmaceutical agent consumed abundantly and

---

* Corresponding authors.
E-mail address: annjurek@pg.edu.pl (A. Zielińska-Jurek).

https://doi.org/10.1016/j.seppur.2023.123320
Received 19 December 2022; Received in revised form 21 January 2023; Accepted 28 January 2023
Available online 1 February 2023

possesses a highly stable nature, making its degradation with conventional water treatment technologies limited. Acetaminophen can cause cardiovascular, gastrointestinal, kidney diseases, and its metabolites may induce mutagenic effects in human cells [7]. Carbamazepine - dibenzoazepine derivative with antiepileptic and psychotropic activity is also well established in treating severe pain syndromes associated with neurological disorders, such as trigeminal neuralgia. Carbamazepine shows low sorption properties and high persistence to biodegradation [8]. Both pharmaceuticals are examples of active pharmaceutical ingredients frequently detected in WWTP effluents, surface waters, groundwater, and occasionally in drinking water in Europe, America, and Asia [9,10]. Furthermore, these pharmaceuticals may have chronic and synergistic ecotoxicological effect in the mixture with other non-steroidal anti-inflammatory drugs [11,12]. Regarding the toxic effects, including bioaccumulation, the most important requirement is the removal of this drugs residues from aquatic systems.

Commonly used methods, including biodegradation [10], chemical oxidation in the presence of persulfate [13], or chlorine [14], are still far from satisfactory concerning the removal of carbamazepine and can generate toxic chlorinated by-products, such as trichloroacetic acid, dichloroacetonitrile, and trichloronitromethane [15].

Recently, advanced oxidation processes (AOPs), including photocatalysis, ozone-based processes such as O_3/H_2O_2 or O_3/UV systems, and Fenton/Fenton-like reactions, are considered the most effective technologies for the treatment of waters containing trace amounts of pharmaceutical pollutants. AOPs are based on the chemistry of hydroxyl radicals ($^{\cdot}OH$), which are non-selective reactive species able to oxidize persistent organic pollutants into non-toxic susceptible to biodegradation intermediates or mineral end-products, yielding CO_2 and inorganic ions [16]. De Luna et al. [17] reported the degradation of acetaminophen by Fenton oxidation in the presence of high concentrations of H_2O_2 and Fe^{2+}. The reaction mixture containing Fe^{2+} ions as catalyst showed 100 % degradation in less than 40 min of process. Furthermore, Fenton-like oxidation is reported as an effective method for CBZ degradation in aqueous solutions under simple operational conditions and within a short time [18]. However, the main drawbacks are the strong acid environment (pH of 3–4) required for the best performance, the relatively high cost of reagents consumption, and the production of ferric sludge [18,19]. Ozone-based processes are capable of the efficient removal of pharmaceuticals [20]. However, they may generate toxicity due to detrimental degradation by-products formation caused by incomplete mineralization. Moreover, the operational costs are often relatively high due to high energy and chemical consumption [16,21].

Among the advanced oxidation processes, heterogeneous photocatalytic oxidation of persistent organic pollutants is considered a sustainable water purification technique since many recalcitrant organic compounds at low concentrations can be oxidized at room temperature in the presence of a semiconductor photocatalyst. At present, the need to develop green, solar-induced chemical processes, such as photocatalysis, is limited by low photoactivity under UV–vis (solar) light, reduced quantum efficiency, and a high recombination rate of photogenerated charge carriers [22,23]. Different types of photocatalysts have been reported to successfully degrade the contaminant molecules from the aqueous phase. Titanium(IV) oxide is widely used in photocatalytic processes due to its chemical and physical stability, low cost, and strong oxidizing properties. Despite the numerous advantages, TiO_2 can be activated almost only by ultraviolet light due to its wide bandgap of about 3.2 (eV).

In order to enhance the performance of semiconductor nanostructures, a suitable architecture, which integrates the usually incompatible features of large specific surface area, high charge-carrier mobility, low electron-hole recombination rate, is highly demanded. In view of this, ultrathin 2D TiO_2 is a promising photocatalytic material that provides many active sites for photocatalytic reactions, allowing the facile adhesion of organic molecules and improved functionality [24,25]. Furthermore, TiO_2 nanosheets minimize the diffusion distance, which photoinduced electron-hole pairs overcome before reaching the solid-water interface, providing a charge transport pathway. Despite the 2D nanosheet structures offer much improvement in the photocatalytic process compared to the bulk 3D TiO_2 crystals, the quantum size effects within the small thickness of the TiO_2 nanosheets may lead to lowering the crystallinity and enlarging the Eg value. Overcoming the limitations related to the reduced spectral activation and recombination between photogenerated electrons and holes, which is often the largest hindrance in photocatalytic efficiency, the aim of the present study was the preparation of 2D TiO_2-based hybrid photocatalyst with improved photocatalytic activity by heterojunction nanolayered TiO_2 with other electron donor semiconductor material.

Recently, 2D graphene-based materials have attracted much attention as an additive photocatalyst for solar light-driven photodegradation of organic pollutants. For example, graphitic carbon nitride (g-C_3N_4) has great potential to work as an efficient, multifunctional material with a medium bandgap of 2.7 (eV), high stability, and photocatalytic activity in the visible light range [26]. Cao et al. [27] reported that nitrogen vacancies graphitic carbon nitride (NV-g-C_3N_4) enhanced the photodegradation efficiency of CBZ since N-vacancies served as electron traps, thus hindering electron-hole recombination. Tubular graphitic carbon nitride (g-C_3N_4) modified with carbon quantum dots (CQD) effectively improved the CBZ photodegradation due to the hindrance effect of CQD in the e^--h^+ recombination [28]. A photocatalyst configuration of TiO_2/graphene/g-C_3N_4 was demonstrated to significantly degrade acetaminophen under simulated solar light irradiation using hydroxyl radicals ($HO^{\bullet}$) and superoxide radicals ($O_2^{\bullet -}$) as oxidizing species. After 120 min of irradiation, 100 % of ACT was degraded, and TOC removal was above 70 % [29]. Combining g-C_3N_4 with inorganic semiconductor such as TiO_2 significantly decreases the recombination rate of electrons and holes [26,30]. Moreover, the heterojunction between g-C_3N_4 and TiO_2 increases the composite interfacial contact area, making more efficient charge transfer at the interface [30]. Zhou et al. [31] reported that a Z scheme 2D nanosheet/nanotube g-C_3N_4/TiO_2 demonstrated high performance in the degradation of rhodamine B (RhB) and tetracycline hydrochloride under visible light range. Furthermore, in the study performed by Chen and co-workers, 3D g-C_3N_4/TiO_2 photocatalyst degraded 87 % of ibuprofen (5 mg/L) from the model solution within 60 min in the presence of visible light irradiation [32]. Besides, the combination of g-C_3N_4/TiO_2 with different chemical elements is reported to improve the photocatalytic activity of heterocomposite. Non-metal doping elements (C, B) [33], (C, N) [34], (P, O)[35], and (N, S) [36] have been reported to improve the photocatalytic activity of g-C_3N_4/TiO_2 according to applications in water splitting and photodegradation of methylene blue (MB), enrofloxacin, rhodamine B (RhB) and Cr(VI) reduction.

In the present study, the 2D TiO_2-based hybrid photocatalysts were prepared for the first time by heterojunction of layered TiO_2 obtained by fluorine-free lyophilization method and modified with multi-anion doped g-C_3N_4. The as-obtained anatase nanosheets were used as building blocks for hybridization with graphitic carbon nitride to enhance photocatalyst performance. Furthermore, to improve the properties of the 2D TiO_2/g-C_3N_4 composite, precursors of phosphorus and sulphur were introduced into the structure of g-C_3N_4. The addition of sulfur in the g-C_3N_4 increased the porosity of the surface since it homogeneously substitutes the lattice nitrogen (N), while the addition of phosphorus (P) increased the separation efficiency of photogenerated electrons and holes and decreased the energy bandgap of semiconductor [37,38]. Even though research studies have been reported on the separate use of phosphorus and sulfur for improving the photocatalytic activity of carbon nitride-based photocatalyst and TiO_2, no studies have focused on the synthesis and application of 2D TiO_2 modified with co-doped (P, S)-g-C_3N_4.

The (P, S)-doped g-C_3N_4 combined with 2D TiO_2 with a mass ratio of (P, S)-g-C_3N_4 to 2D TiO_2 of 2.5, 5, 10, and 20 wt% were applied for carbamazepine and acetaminophen photocatalytic degradation under simulated solar light. The reaction kinetics and the reusability of the prepared photocatalysts were also investigated, and possible mechanisms and photodegradation pathways of carbamazepine (CBZ) and acetaminophen (ACT) were proposed according to identified intermediates and DFT calculations.

2. Experimental

2.1. Materials

In this study, thiourea (99 %), melamine (99 %), diammonium hydrogen phosphate $(NH_4)_2HPO_4$ (≥98 %), and titanium oxysulfate (≥29 % Ti as (TiO_2), basis, technical) were purchased from Sigma Aldrich. Ammonia solution (25 %), hydrogen peroxide H_2O_2 (30 %), and methanol were obtained from (POCH S.A.). The selected organic pollutant of carbamazepine and acetaminophen (99 % pure Bio extra) were purchased from Sigma Aldrich. The anionic surfactant of sodium dodecyl sulfate (SDS; 85 % pure) was purchased from (ACROS-Organics). The scavengers of ammonium oxalate, para benzoquinone (P-BQ), sodium azide (NaN_3), silver nitrate ($AgNO_3$), and isopropanol were provided from Sigma Aldrich and used without any further purification. HPLC gradient grade, acetonitrile, and orthophosphoric acid were provided by Merck.

2.2. Synthesis of (P, S) co-doped g-C_3N_4

Phosphorus and sulfur co-doped graphitic carbon nitride was obtained by thermal treatment. In this regard, 7.5 g thiourea, 7.5 g melamine, and 1.36 g $(NH_4)_2HPO_4$ were mixed and grounded to form a powder. The obtained powder was heated at 550 °C for 4 h with a rate of 2 $°C \cdot min^{-1}$. Calcination enables the linkage of P and S atoms in the g-C_3N_4 network. After thermal treatment, the obtained agglomerates were grounded into a powder and heated at 500 °C for 3 h, with a rate of 5 $°C \cdot min^{-1}$. The final obtained product was a fine light yellow powder of (P, S)-doped g-C_3N_4.

2.3. Synthesis of 2D TiO_2 nanosheets

The TiO_2 nanosheets were prepared using the freeze-drying method as a green concept for the synthesis. Titanium oxysulfate (10 g) was dissolved in 300 cm^3 of deionized water at 40 °C. Then, the solution was cooled down until it reached 5 °C and the ammonia solution was added dropwise until a pH of 9. The obtained white precipitate was centrifugated, washed, and re-suspended in 300 cm^3 of deionized water. Furthermore, 60 cm^3 of 30 % aqueous H_2O_2 was added to the suspension, the suspension turned yellow, and the pH dropped to 2. The solution was aged at 5 °C to form a gel, and then it was frozen using liquid N_2. Further, the sample was placed into a freeze-dryer and lyophilized. In the last step, the dry powder was calcinated at 700 °C to form the final TiO_2 nanosheets.

2.4. Synthesis of (P, S) co-doped g-C_3N_4/TiO_2

The (P, S) co-doped g-C_3N_4 was coupled with 2D TiO_2 in 50 cm^3 of methanol in the presence of an anionic surfactant, SDS (sodium dodecyl sulfate salt, 2 % w/w). The mixture was sonicated for 30 min. Finally, the suspension was washed 3 times with deionized water and dried in the oven at 100 °C for 4 h. Four different types of composite with different mass ratios of (P, S) co-doped g-C_3N_4 (2.5; 5; 10 and 20 % w/w) to 2D TiO_2 were prepared.

2.5. Characterization of photocatalysts

The phase composition of prepared photocatalysts was analyzed using X-ray powder diffraction (Cu Kα radiation, Rigaku MiniFlex 600 X-ray diffractometer). Data samples were measured in the 2Θ range 5-80° with a scan speed of 1°/min and scan step of 0.01°. The analyses were performed based on the International Centre for Diffraction Data (ICDD) database. Debye-Scherrer equation was used to estimate the particle size of the photocatalyst, and it consists of the following $D = K\lambda/\beta\cos\theta$, where K stands for Scherrer constant, λ presents the wavelength of the X-ray beam, β is the full width at half maximum of the peak, and lastly, the Bragg angle is represented by theta (θ).

The Brunauer-Emmet-Teller (BET) surface area of the photocatalysts was investigated using Micromeritics Gemini V (model 2365) (Norcross, GA, USA). Before performing nitrogen adsorption measurements, the prepared samples were degassed at 200 °C for 2 h. The diffuse reflectance (DR) spectra were measured by UV–vis spectrophotometer (Thermo Fisher Scientific Evolution 220) using $BaSO_4$ as a standard. The bandgap energy was calculated using the Kubelka-Munk function.

Microscopic measurements were performed using scanning electron microscope (Quanta 3D FEG, FEI Europe) with secondary electron (SE) detector (Everhart–Thornley detector) and transmission electron microscope (model Tecnai F20 X-Twin) coupled with the spectroscopic techniques (EDS, EELS). In TEM mode, a dark field (DF) detector was used for imaging. In the STEM mode, a high angle annular dark field (HAADF) detector was used for imaging, and energy dispersive spectrometer (EDS) RTEM SN9577+, by EDAX (Pleasanton, USA), or parallel electron energy loss spectroscopy (PEELS) by Gatan (Pleasanton, USA) was used to analyze the elements.

The chemical states on the surface of photocatalysts were examined by X-ray photoelectron spectroscopy (XPS). X-ray photoelectron spectroscopic (XPS) measurements were performed using a PHI 5000 VersaProbe (ULVAC-PHI) spectrometer with monochromatic Al K_α radiation ($h\nu = 1486.6$ eV) from an X-ray source operating at 100 μm spot size, 25 W and 15 kV. The high-resolution (HR) XPS spectra were collected with the hemispherical analyzer at the pass energy of 117.4 and the energy step size of 0.1 eV. The X-ray beam was incident at the sample surface at the angle of 45° with respect to the surface normal, and the analyzer axis was located at 45° concerning the surface. The CasaXPS software was used to evaluate the XPS data. Deconvolution of all HR XPS spectra was performed using a Shirley background and a Gaussian peak shape with 30 % Lorentzian character.

The Fourier Transformer Infrared Spectroscopy (FTIR) measurements were performed using a Nicolet iS10 FTIR spectrometer in the scan range of 400–4000 cm^{-1} as the diffuse reflectance for powder samples in KBr with the resolution of 2 cm^{-1}.

The zeta potential analyses were performed using Nano-ZS Zetasizer dynamic light scattering detector (Malvern Instruments UK) equipped with a 4.0 mW internal laser.

X-ray fluorescence spectroscopy (XRF) using a WDXRF S8 TIGER analyzer (Bruker, S8 TIGER, Bruker, Karlsruhe, Germany) was employed to evaluate the sulfur content in (P, S)-g-C_3N_4. The analyses were performed according to the standard PN-EN 15309:2010.

Diffuse reflectance spectra (DR/UV–vis) in the 200–800 nm range were recorded and converted to absorption using ThemoScientific Evolution 220 Spectrophotometer (Waltham, MA, USA) equipped with PIN-757 integrating sphere. The optical bandgap of 2D TiO_2 and 2D TiO_2/g-C_3N_4 composites were calculated from the Kubelka-Munk function of $\alpha h\upsilon = A(h\upsilon - E_g)^n$, where α is the absorption coefficient, hυ is the photon energy (eV), h is Plank constant, υ is the frequency (s^{-1}), A is a constant, n is equal to 0.5.

The Raman spectra of the photocatalysts were investigated using the Renishaw InVia Raman spectrometer equipped with an IR laser diode and a CCD camera as a detector. The polarized Raman spectra were excited with the IR diode laser emitting at 830 nm (1 mW) and recorded in a single scan with a 30 s exposure time using a 20 × LWD objective.

Emissions and decay times measurements were performed using an excitation source consisting of a femtosecond laser (Coherent Model "Libra") coupled to the optical parametric amplifier (Light Conversion Model "OPerA"). The system delivers 100 fs pulses at a repetition rate regulated up to 1 kHz at a wavelength tuned between 230 and 2800 nm.

The luminescence spectra and decay curves were recorded with a grating spectrograph (Princeton Instr. Model Acton 2500i) coupled to a streak camera (Hamamatsu Model C5680) with a temporal resolution of 20 ps.

The Mott-Schottky analysis was performed to determine the flat band (F_b) potential of the photocatalyst. The EIS data were recorded from the anodic towards a cathodic direction using Potentiostat/Galvanostat Autolab PGSTAT204 (Metrohm Autolab) with a Na_2SO_4 (0.5 M) as an electrolyte. EIS data were recorded for the applied frequency of 1000 Hz in the potential range from + 1.0 to − 1.5 V vs. Ag/AgCl. The spectra were run at the frequency range from 20 kHz to 0.1 Hz with a 10 mV amplitude of the alternating current.

The photon flux measurements were performed by UV–vis spectrophotometer (Thermo Fisher Scientific Evolution 220) using $BaSO_4$ as a standard. The wavelength range of 300–400 nm was used to record the absorption spectra for 2D TiO_2 and (P, S)-g-C_3N_4/ 2D TiO_2 (5 %). Optical properties of the best-performing sample (5 % composite) in comparison to the pure 2D TiO_2, following the procedures reported in the literature [39].

2.6. Photocatalytic degradation

The photocatalytic activity was evaluated by the degradation of carbamazepine (CBZ; 14 mg·dm^{-3}) and acetaminophen (ACT; 20 mg·dm^{-3}). Photocatalytic activity for the prepared samples was measured using a photocatalytic set-up in a black box. The pharmaceutical solution was stirred for 30 min in the dark to ensure the equilibrium of adsorption–desorption. After 30 min, the UV–vis irradiation (xenon lamp, 30 mW·cm^{-2}) was introduced into the reactor. The samples were collected within the time frame of −30, 0, 15, 30, 60, and 120 min. Quenching experiments were performed to identify the main active species in the photocatalytic process. In this regard, 1 mM of isopropanol ($^{\bullet}$OH scavenger), ammonium oxalate (h^+ scavenger), benzoquinone BQ ($O_2^{\bullet-}$ scavenger), sodium azide ($^1O_2$ scavenger), and silver nitrate (e^- scavenger) was added in the reaction solution of selected pharmaceutical. Photodegradation efficiency was monitored using a high-performance liquid chromatography system (HPLC, model Shimadzu LC-6A) equipped with a photodiode array detector (SPD-M20A) and C18 column (Phenomenex Gemini 5 µm; 150 × 4.6 mm) working at 45 °C. For HPLC measurements of carbamazepine (CBZ), the mobile phase consisted of (v/v) 60 % H_2O, 0.5 % orthophosphoric acid (85 % w/w solution), and 39.5 % acetonitrile was used at a flow rate of 1.5 cm^3·min^{-1}. On the other hand, the mobile phase for ACT consisted of (v/v) 30 % methanol (MeOH), 69.9 % H_2O, and 0.1 % formic acid (HCOOH) with a flow rate of 0.8 cm^3·min^{-1}.

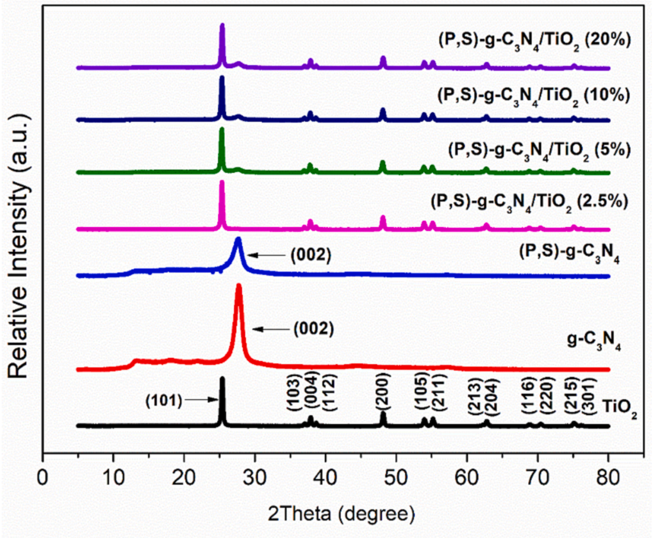

Fig. 1. XRD diffraction patterns of prepared photocatalysts.

The synergy values were calculated to evaluate whether the heterocomposite formation is efficient in the degradation of CBZ and ACT, as compared to the semiconductors separately. Additionally, these values can provide the information regarding which of formed heterocomposites demonstrates greater efficiency. Synergy coefficients were calculated accordingly to the given formula: $S = \frac{k(heterocomposite)}{k(P,S-g-C_3N_4)+k(2DTiO_2)}$, where k (min^{-1}) is the rate constant obtained for degradation of pharmaceutical in the presence of heterocomposite, and rate constants obtained for degradation of pharmaceutical for semiconductors separately.

Additionally, the mineralization efficiency of CBZ and ACT was studied as total organic carbon (TOC) removal using the Shimadzu TOC-L apparatus. Quantitative analyzes were performed using the external calibration method with a standard compound obtained by Sigma-Aldrich.

Optical properties of the photocatalyst suspensions were determined for the best-performing composite and 2D TiO_2 as a control to check for possible differences in the photon-absorption ability of both materials. Experimental determination of the mass-specific extinction/absorption coefficients was based on the absorbance values obtained from direct/scattered transmittance measurements through the suspensions with different powder concentrations [39]. Measurements were performed in the wavelength range of 300–400 nm, and final values were obtained as an average value in this region. Obtained optical parameters of both samples were used to numerically model the local volume rate of photon absorption (LVRPA), following the six-flux model approach [40]. Detailed calculations followed the procedure reported by Acosta-Herazo et al. [41]). The applied scattering probabilities in the forward, backward and side directions were 0.754, 0.133 and 0.028, respectively, following the Henyey-Greenstein phase function, as suggested for the TiO_2 materials [41]. Integration of the LVRPA over the cross-section of the rector was performed to calculate the total rate of photon absorption (TRPA) for a unit length of the reactor. A comparison of the TRPA value with the incident photon flux was used to estimate the total number of absorbed UVA photons during the process for both materials.

Identification of intermediates was performed using the high-performance LC-MS system, which consisted of an HCT Ultra spectrometer (Bruker Daltonics, Billerica, Massachusetts, US) with an ESI source coupled with an Agilent 1200 liquid chromatograph (Agilent Technologies, Santa Clara, California, US). Chromatographic separation was conducted on Eclipse XDB-C8, 4,6 × 150 mm, 5 um (Agilent) column. Mobile phase A was water with 0.1 % formic acid and phase B acetonitrile with 0.1 % formic acid. Gradient program was as follows: 0 min – 1 % B, 5 min – 1 % B, 25 min – 90 % B, 30 min – 90 % B, 35 min – 1 % B. The flow was set at 0.4 ml/min, and the injection volume was 50 µl. Column oven temperature was set to 25 °C and UV chromatograms were recorded at: 220, 246 and 254 nm. Spectra were acquired in positive and negative ESI mode, the capillary voltage was set at 113 V, the scanned mass range was 50–850 *m/z* and the accumulation time was 200,000 ms. The parameters capillary voltage, drying gas flow, nebulizing gas and source temperature was respectively: 4.0 kV, 10 L min − 1, 30 psi and 350 °C. Helium (99.999 %) was used as the collision gas in the ion trap. The mass spectrometer was operated in full scan and single ion monitoring modes (SIM).

2.7. Computational analysis of degradation products

Computational analysis of the possible degradation by-products was performed at the density functional theory level (DFT) using Orca 5.0.3 software package [42]. All considered structures were modeled using B3LYP functionals [43] with the aug-cc-PVDZ basis set and included the conductor-like polarizable continuum model (CPCM) to account for the water matrix effect. The geometry of each compound was optimized to the default convergence thresholds of energy, gradient, and

Table 1
Characterization of the obtained photocatalysts. The surface area, pore volume and bandgap energy.

Photocatalyst	Surface area ($m^2 \cdot g^{-1}$)	Total pore volume ($cm^3 \cdot g^{-1}$)	Band gap energy (eV)
2D TiO_2	10.98	0.018	3.15
g-C_3N_4	16.56	0.0084	2.60
(P, S)-g-C_3N_4	17.41	0.0084	2.42
(P, S)-g-C_3N_4/TiO_2 (2.5 %)	17.58	0.0087	3.00
(P, S)-g-C_3N_4/TiO_2 (5 %)	17.97	0.0087	2.90
(P, S)-g-C_3N_4/TiO_2 (10 %)	17.29	0.0086	2.85
(P, S)-g-C_3N_4/TiO_2 (20 %)	17.27	0.0086	2.85

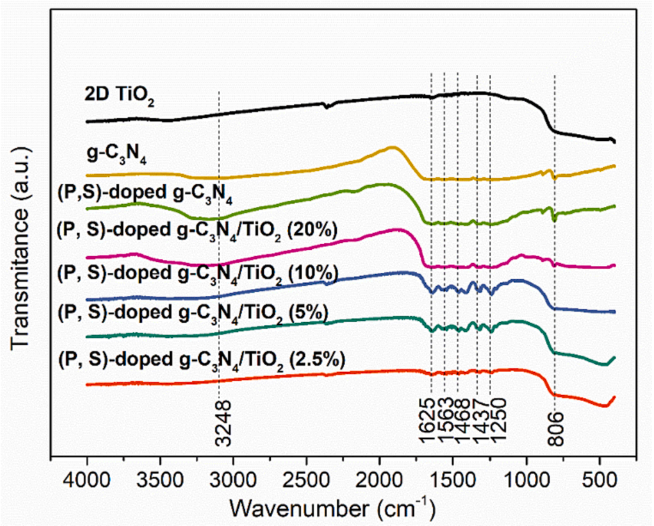

Fig. 2. The FTIR spectra for the obtained photocatalysts.

displacement. The energy effect of the possible reaction was calculated as the products-substrates energy difference, using O_2 and H_2O molecules to balance the stoichiometry (during the photocatalytic process, a number of reactive oxygen species are expected to form and react with pollutant, however O_2 and H_2O are both primary substrates, as well as final re-created products in the ambient conditions after the process). For the selected compounds, additional time-dependent DFT calculations were performed at the optimized geometry to simulate expected absorption spectra. Moreover, in the case of two carbamazepine structures, possible rearrangement of the molecule was studied using nudged elastic band method to determine the possible energy barrier and transition state of such a process. Finally, calculations of Fukui functions were performed based on the electron density maps for neutral, N + 1 and N-1 electron states (N is a number of electrons) of the acetaminophen dimer to possibly suggest positions of the further reactive species attack.

3. Results and discussion

3.1. *Characterization of obtained photocatalysts*

The results of X-ray diffraction (XRD) analysis of 2D TiO_2, (P, S)-doped g-C_3N_4, and (P, S)-doped g-C_3N_4/TiO_2 composite are presented in Fig. 1. The 2D TiO_2 photocatalyst exhibited characteristic peaks indexed to the corresponding anatase phase planes (JCPDS 21-1272). The most intensive peak of the (1 0 1) diffraction plane of TiO_2 at 25.53° 2θ was noticed for 2D TiO_2 and all obtained (P, S)-doped g-C_3N_4/TiO_2 composites. The distinct peak at 27.71° 2θ with the corresponding (0 0 2) diffraction plane of graphitic carbon nitride is ascribed to the interlayer stacking structure of the aromatic compound, and a signal at 13.21° 2θ with (1 0 0) plane is attributed to the in-plane repeat motif of tri-s-triazine [44]. The diffraction plane (1 0 0) at 13.21° 2θ was observed only for the g-C_3N_4 sample and started to vanish in the composites indicating the complete unification of both phases. Identified diffraction peaks of both (P, S)-doped g-C_3N_4 and 2D TiO_2 are observed in all samples of (P, S)-doped g-C_3N_4/TiO_2 composites, except (P, S)-doped C_3N_4/TiO_2 (2.5 %), where the peak was not detectable, but the presence of (P, S)-doped g-C_3N_4 was later confirmed by FT-IR analysis. The crystallite size of (P, S)-doped g-C_3N_4 was 15 nm, and 2D TiO_2 was about 33 nm.

Furthermore, the surface area of doped graphitic carbon nitride and 2D TiO_2 was found to be 17.41 $m^2 \cdot g^{-1}$ and 10.98 $m^2 \cdot g^{-1}$ (see Table 1). The composites of (P, S)-doped g-C_3N_4/TiO_2 possessed a surface area of about 17–18 $m^2 \cdot g^{-1}$ similar to that of (P, S)-g-C_3N_4. Furthermore, the pore volume for 2D TiO_2 was about 0.018 $cm^3 \cdot g^{-1}$, and the pore volume for (P, S)-g-C_3N_4 was 0.0087 $cm^3 \cdot g^{-1}$. The pore volume of composites was comparable to that of (P, S)-doped g-C_3N_4.

Three different bands can be distinguished at FTIR spectra of g-C_3N_4 and (P, S)-doped g-C_3N_4, as presented in Fig. 2. The broad peak at 3248 cm^{-1} is attributed to the stretching vibrations of the N—H group. The stretching and rotation vibrations of C—N and C═N of g-C_3N_4 were detected in the region of 1250–1625 cm^{-1}, whereas s-triazine ring vibrations are observed at 806 cm^{-1} [45]. For the 2D TiO_2 sample, the broad band between 500 and 750 cm^{-1} is ascribed to the stretching mode of the Ti-O-Ti bridge [32]. The characteristic range band between 1250 and 1625 cm^{-1} is noticed for all composite samples, indicating thus the presence of (P, S)-doped g-C_3N_4 at the surface of 2D TiO_2. Furthermore, the presence of (P, S) was proved through XPS and XRF analyses.

The structure of photocatalysts was further characterized by microscopy analyses, and the results are presented in Fig. 3. The SEM images showed the platelet-shaped of (P, S)-g-C_3N_4 and 2D planar nanosheets of anatase (Fig. 3 a-b). The TEM microscopic analyzes confirmed the formation of the 2D TiO_2 structure of anatase (Fig. 3d). The FFT analysis of the noise-refined TEM lattice fringe images (Fig. 3e) revealed lattice spacing values of 0.19 nm, 0.235 nm, 0.368 nm, 0.349 nm, which are in good agreement with the crystal plane spacing d(hkl) of (2 0 0), (0 0 1), (0 1 0), (1 0 1) of anatase, respectively, thus indicating that the zone axis is [0 0 1] [46,47]. In Fig. 3 f-g, magnification of (P, S)-g-C_3N_4/TiO_2 (5 %) obtained from melamine as a precursor showed that (P, S)-g-C_3N_4 platelet-like particles are almost homogeneously well dispersed throughout the structure of anatase nanosheets. According to previous studies, the precursor used for the synthesis of carbon nitride (g-C_3N_4) is responsible for the morphology of produced photocatalyst. It has been reported that thiourea and urea mainly give exfoliated thin and thick planar sheets, while implementation of cyanamide and melamine precursors manifests into platelet-like shape particles and planar sheet-type morphology [48]. Furthermore, the EDX elemental composition analysis confirmed the successful doping of (P, S)-g-C_3N_4/TiO_2 (5 %) heterocomposite with P atoms. The lack of S atoms is due to the small amounts of S in the composition, but the presence of sulfur atoms in the lattice of nanocrystals was further proved by XPS and XRF analyses. Additionally, particle size distribution analysis showed the majority of nanoparticles in the range of 35–42 nm (Fig. 3g).

The survey XPS spectra of 2D TiO_2 and 2D TiO_2-based composites containing from 2.5 % to 10 % of (P, S)-doped g-C_3N_4 recorded in the binding energy (BE) range of 0 to 1300 eV are presented in Figure S1 in the Supporting Material. The peaks were identified in the same positions for all the composite materials. The only difference is the third identified chemical bond in N 1s spectra, where instead of NO_2, it was shown to be C-NH_2 at the position of 401.99 eV. Related to the slight shifts of peaks, it can be explained by the differences in the content of (P, S)-doped g-C_3N_4 in the composites of (P, S)-g-C_3N_4/TiO_2 (2.5 %), (P, S)-g-C_3N_4/

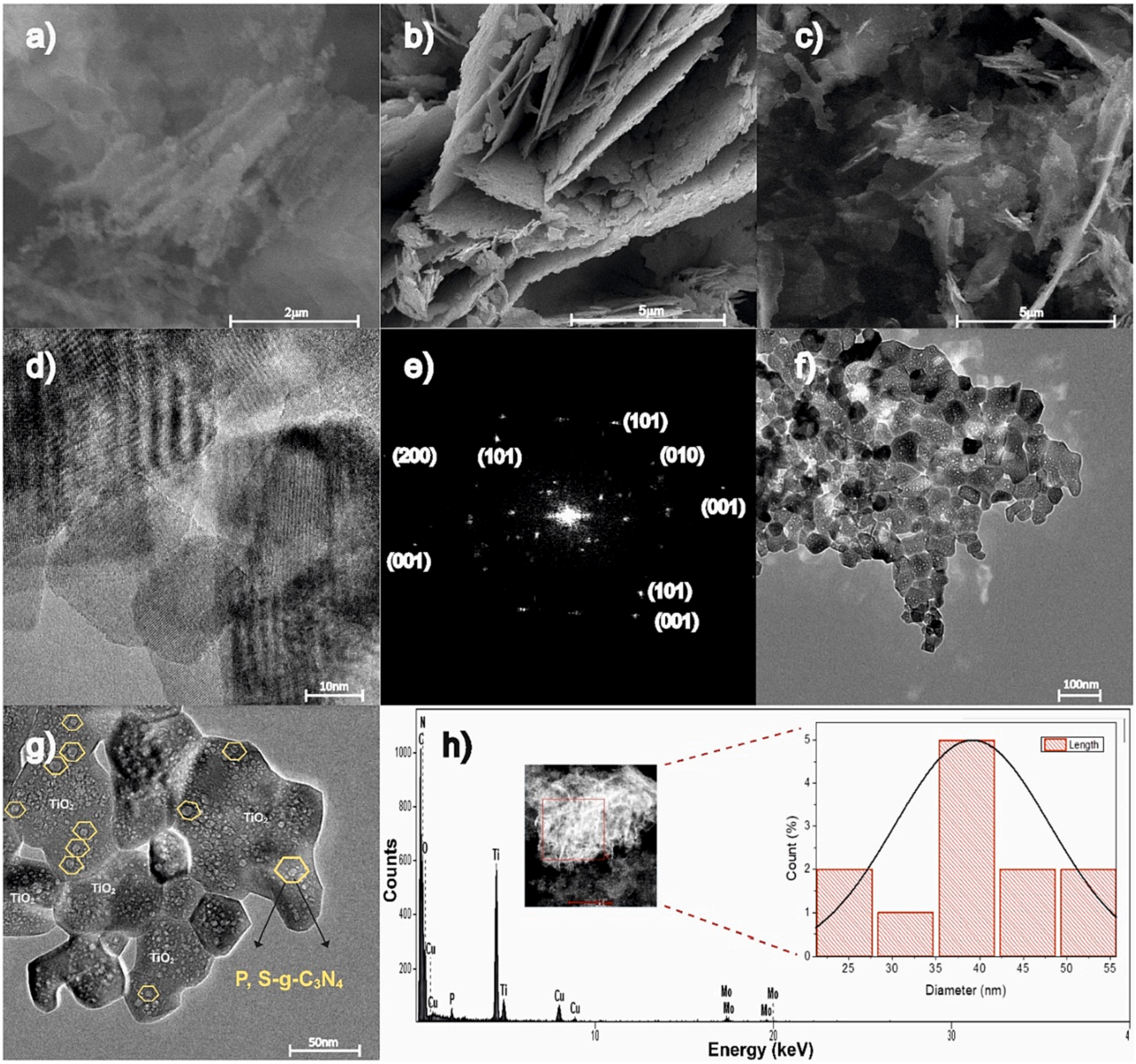

Fig. 3. SEM images of synthesized (P, S)-doped g-C_3N_4 (a), 2D TiO_2 (b), (P, S)-doped g-C_3N_4/TiO_2 (5 %) (c), TEM and corresponding FFT image of 2D TiO_2 nanosheets (d, e), TEM images of (P, S)-doped g-C_3N_4/TiO_2 (5 %) (f, g), EDX elemental composition graph and size distribution graph for (P, S)-doped g-C_3N_4/TiO_2 (5 %) (h).

TiO_2 (5 %) and (P, S)-g-C_3N_4/TiO_2 (10 %).

As presented in Fig. 4, the characteristic peaks for Ti 2p are observed at a binding energy of 464.5 eV (Ti $2p_{1/2}$) and 458.5 eV (Ti $2p_{3/2}$) and are related to Ti^{4+} [49]. The O 1s region could be deconvoluted for three peaks. The major peak at 530.16 eV is related to oxygen in the TiO_2 crystal lattice (Ti—O—Ti). The less intense peaks at 530.96 eV and 531.84 eV are assigned to oxygen in O—H and C═O bonds [36].

The C 1s region could be deconvoluted for three peaks at 284.8, 286.11, and 288.35 (eV) associated with sp^2 hybridization of C═C bonds, chemical bonding of C-O and sp^2 hybridization of C in N═C (—N)$_2$ bond, which directly proved the presence of graphitic carbon nitride in the composition [50]. The observed signals around 398 eV and 400 eV corresponded to the presence of C—N bonding in the carbon nitride network and tertiary nitrogen groups C—(N)$_3$. Fig. 4e showed that binding energies of 133.8 eV and 134.72 eV corresponding to the peaks of P $2p_{3/2}$ and P 2 $p_{1/2}$ are attributed to the P—N bond, indicating the substitution of phosphorus in the carbon position and its covalently bonding with the nitrogen of the g-C_3N_4 framework [51]. The XPS spectra of S 2p showed the presence of two small and broad peaks at 168.64 eV and 169.84 eV (Fig. 4f). Generally, the presence of sulfur can be detected as S 2p at binding energies of 165 and 166 eV [52]. If the obtained value of binding energy is lower than 165 eV, it suggests for S-doped in the position of nitrogen with a rise in the S—C bond, whereas a higher value indicates for S-doped in the position of carbon, giving thus rise in the S—N bond [52,53]. The (P, S)-g-C_3N_4/TiO_2 heterocomposite formation results from surface modification than doping and substitution of O atoms with (P, S)-atoms in the TiO_2 lattice since Ti—C bonds (459.4 eV), P-Ti bonds (128.6 eV) and Ti-S bonds (163.4 eV) are not observed based on XPS analysis [54–56]. Meanwhile, the XPS analysis for the most active (P, S)-g-C_3N_4/TiO_2 (5 %) photocatalyst confirmed the presence of 25.25 at. % of Ti, 63.60 at. % of O, 7.66 at.% of C, 2.24 at.% of N, 1.05 at.% of P, and 0.21 at.% of S.

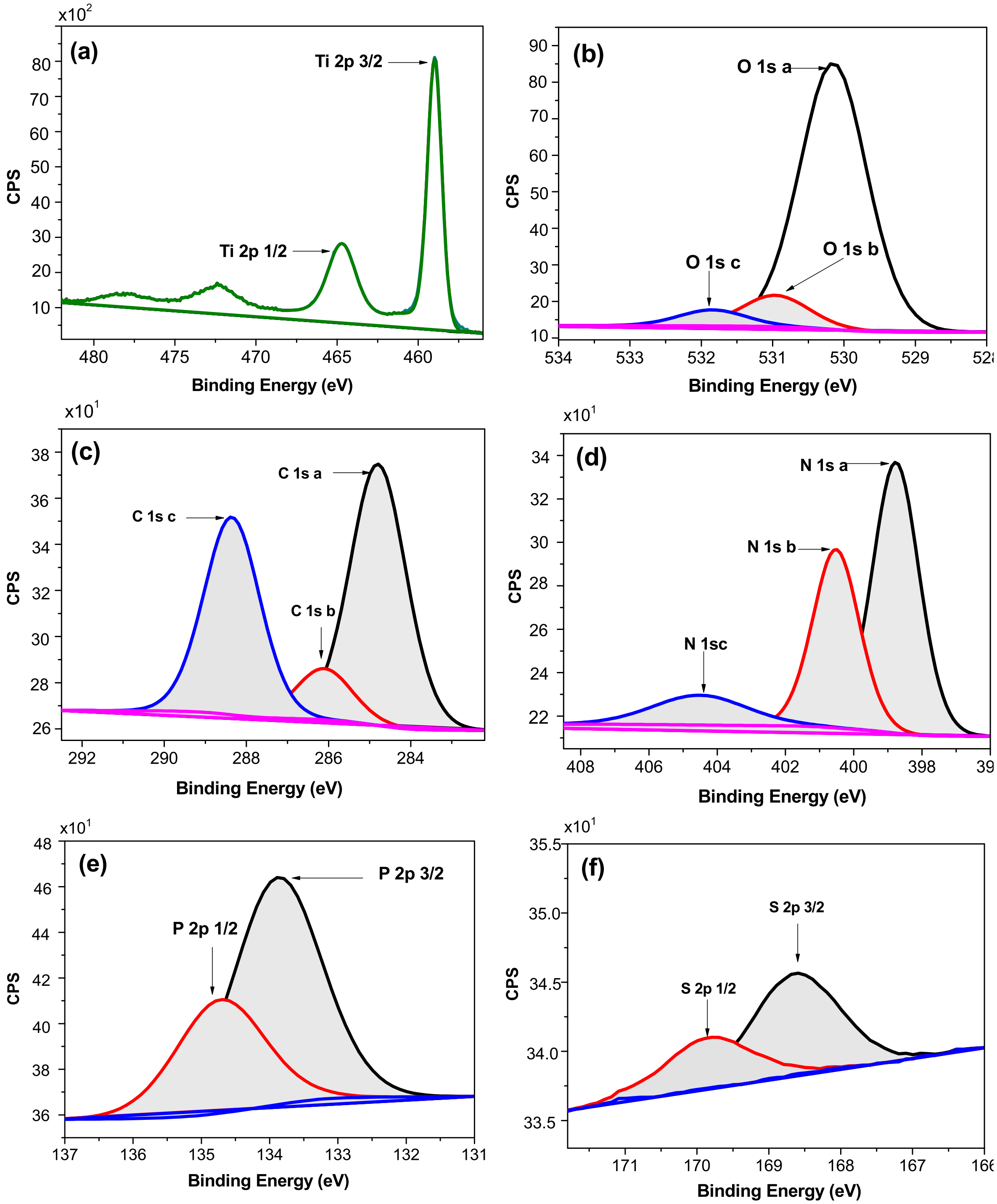

Fig. 4. XPS spectra for Ti 2p (a), O 1s (b), C 1s (c), N 1s (d), P 2p (e), and S 2p (f) signals with Gaussian fits, respectively.

Additionally, X-ray fluorescence spectroscopy (XRF) confirmed the presence of 0.05 % of sulfur in the (P, S)-g-C_3N_4 composite. The XPS spectra for lower (2.5 wt%) and higher amounts (10 wt%) of (P, S)-g-C_3N_4 in the composite of (P, S)-g-C_3N_4/TiO_2 are shown in Figures S2 and S3 in the Supporting Material.

The Raman spectra of 2D TiO_2, (P, S)-doped g-C_3N_4, and (P, S)-doped g-C_3N_4/TiO_2 (5 %) photocatalysts are presented in Fig. 5. The space group of the tetragonal anatase is I41/amd, and the local symmetry is D2d which, after group factor analysis, led to the conclusion that in the Raman spectrum, six basic Raman-active modes (A1g + 2B1g + 3Eg) should be observed. The Raman spectrum of TiO_2 showed five bands at 141 (Eg), 195 (Eg), 395 (B1g), 515 (A1g), and 639 (Eg) cm^{-1}. The sixth band, usually observed at about 513 cm^{-1} (A1g), may not be noticed due to the broadening of the band observed at 515 cm^{-1}. The Raman spectrum of (P, S)-g-C_3N_4 consisted of several peaks of g-C_3N_4 at 478, 708, 752, 982, 1236, and 1315 cm^{-1}, where two of them were most distinguished at 708 and 1236 cm^{-1}, respectively. The peak observed at 708 cm^{-1} can be assigned as the layer–layer deformation vibrations and at 1236 cm^{-1} to the =C (sp^2) bending vibration [57]. In the hybrid (P, S)-g-C_3N_4/TiO_2 material, only 2 at% of g-C_3N_4 was noticed; therefore, the signal is quite weak, but it is still possible to observe a single, small peak at around 708 cm^{-1} on the slope of the TiO_2 Eg band (639 cm^{-1}).

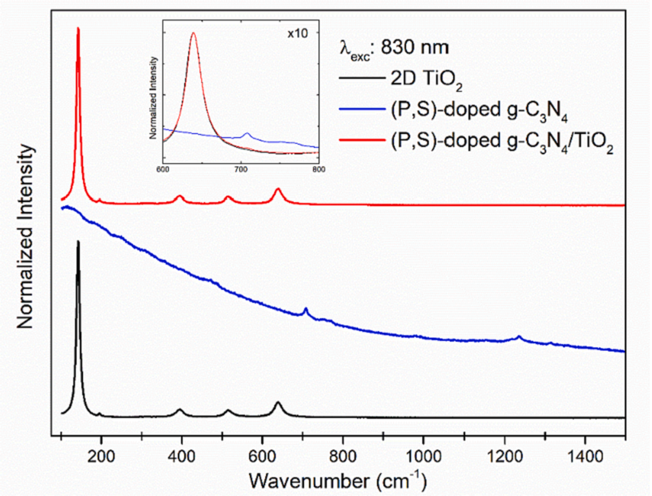

Fig. 5. Raman spectra of the 2D TiO$_2$, (P, S)-doped g-C$_3$N$_{4,}$ and (P, S)-doped g-C$_3$N$_4$/TiO$_2$ (5 %) powders recorded with the 830 nm excitation wavelength.

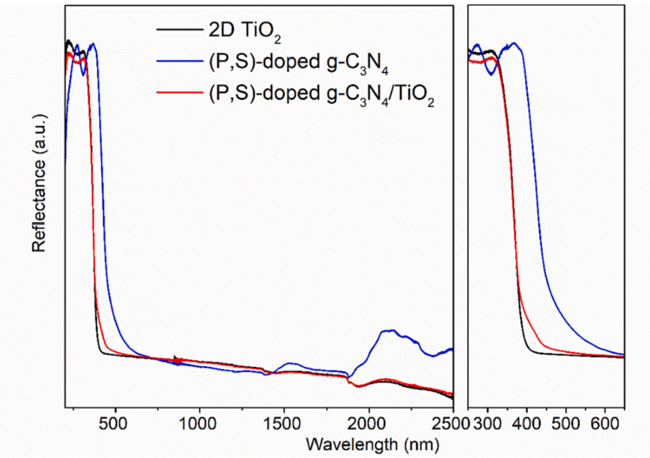

Fig. 6. Reflectance spectra of the TiO$_2$, (P, S)-doped g-C$_3$N$_4$ and (P, S)-doped g-C$_3$N$_4$/TiO$_2$ (5 %) photocatalysts.

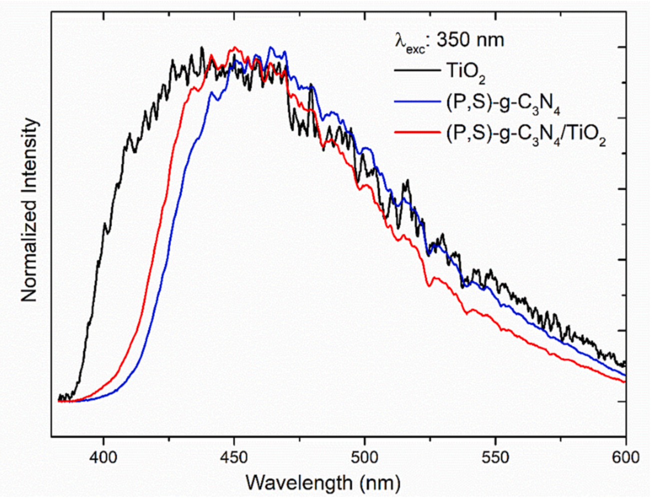

Fig. 7. Luminescence spectra of the 2D TiO$_2$, (P, S)-doped g-C$_3$N$_4$, and (P, S)-g-C$_3$N$_4$/TiO$_2$ (5 %) photocatalysts under UV excitation.

The optical properties of photocatalysts were studied using UV–vis diffuse reflectance spectroscopy and are presented in Fig. 6. The TiO$_2$ nanosheets display a typical absorption edge at about 395 nm, corresponding to the bandgap of 3.15 eV [58]. The reflectance spectra of (P, S)-g-C$_3$N$_4$ consist of a band similar to a typical semiconductor absorption spectrum between 200 and 450 nm, originating from the charge transfer from a populated valence band of a nitrogen atom (2p orbitals) to a conduction band of carbon atom (2p orbitals) of carbon nitride. For the (P, S)-doped g-C$_3$N$_4$ structure, the absorption edge is observed at about 510 nm, corresponding to the bandgap of 2.42 eV, which is redshifted compared to the pure g-C$_3$N$_{4,}$ where the absorption edge is observed at 480 nm (2.60 eV). The stronger visible-light absorption of (P, S)-g-C$_3$N$_4$ showed the possibility of more efficient utilization of sunlight for photocatalysis. In the case of the (P, S)-g-C$_3$N$_4$/TiO$_2$ hybrid material, it can be observed that the absorption band of TiO$_2$ is broadened, and the sideband corresponds to the absorption of (P, S)-g-C$_3$N$_4$.

The emission spectra of all structures showed a broad band in the spectral range from 400 to 600 nm, see in Fig. 7. It can be observed that the 2D TiO$_2$ emission band is broader than the (P, S)-doped g-C$_3$N$_4$ and the hybrid structure of (P, S)-doped g-C$_3$N$_4$/TiO$_2$. For the TiO$_2$ emission spectrum, the high-energy region of the band corresponds to the indirect band-to-band recombination across the bandgap, and the luminescence in the low-energy range is attributed to excitons that result from surface oxygen vacancies and defects. The (P, S)-doped g-C$_3$N$_4$ luminescence spectrum showed the typical band of an organic semiconductor with a strong emission peak at about 470 nm, which is caused by the transition between lone pair to π* conduction band. The hybrid structure emission spectrum showed the combination of the 2D TiO$_2$ and (P, S)-g-C$_3$N$_4$ luminescence properties. The band is narrower, as for (P, S)-g-C$_3$N$_4$, and blueshifted, as for TiO$_2$. It resulted from reducing the electron density of the π state conjugated system or lone pair state of g-C$_3$N$_4$ by the TiO$_2$ particles that were also previously observed for the boron-doped g-C$_3$N$_4$ [59].

The decay times of 2D TiO$_2$, (P, S)-doped g-C$_3$N$_4$ and the hybrid structure were measured using a 50 ns time window (see Fig. 8). In all the cases, non-exponential decay was observed. In the TiO$_2$ powder, the interaction between electrons and holes was weak because of its indirect-gap band structure; therefore, in the decay profile, a rapid decrease in hole population followed by long-lived electron decay is observed [60]. The luminescence decay of (P, S)-g-C$_3$N$_4$ was fitted using three components. The short-living components are associated with the recombination of the electron-hole pairs, and the longer decay can be assigned to the fast separation of electron-hole pairs [61]. Interestingly, although in the (P, S)-doped g-C$_3$N$_4$/TiO$_2$ is only 5 % of (P, S)-g-C$_3$N$_{4,}$ the luminescence decay is more similar to the nitride than to oxide. It can also be observed that the decay times are slightly shorter for the hybrid material than for pure (P, S)-g-C$_3$N$_4$ (Table 2). Another fact worth noticing is that under 405 nm excitation (absorption maximum of (P, S)-g-C$_3$N$_4$ and sideband of (P, S)-g-C$_3$N$_4$/TiO$_{2,}$ the decays are prolonged, and in the case of hybrid photocatalyst can be again observed the long decay component associated with electrons decay (Table 2). From the obtained results, it can be observed that heterojunction formation resulted in better separation of electron-hole pairs.

Fig. 9a shows the Nyquist impedance plot for (P, S)-g-C$_3$N$_4$, 2D TiO$_2$ and (P, S)-g-C$_3$N$_4$/2D TiO$_2$ (5 %). From Nyquist plots, a small semicircular diameter indicates lower e$^-$- h$^+$ recombination and high electrical conductivity. The results suggested that the combination of (P, S)-g-C$_3$N$_4$ and 2D TiO$_2$ reduced the charge transfer resistance and enhanced the separation efficiency of photogenerated charge carriers.

Furthermore, to study the surface properties of (P, S)-g-C$_3$N$_4$, 2D TiO$_2$ and (P, S)-g-C$_3$N$_4$/TiO$_2$ (5 %) photocatalysts, the electrophoretic mobility in a function of pH (zeta potential) was investigated (see Fig. 9b).

For pH < pH$_{IEP}$ the surface of photocatalysts was positively charged, while for pH > pH$_{pzc}$ the surface of the photocatalyst was negatively charged. Regarding the preparation procedure, the pH ranging from 4 to

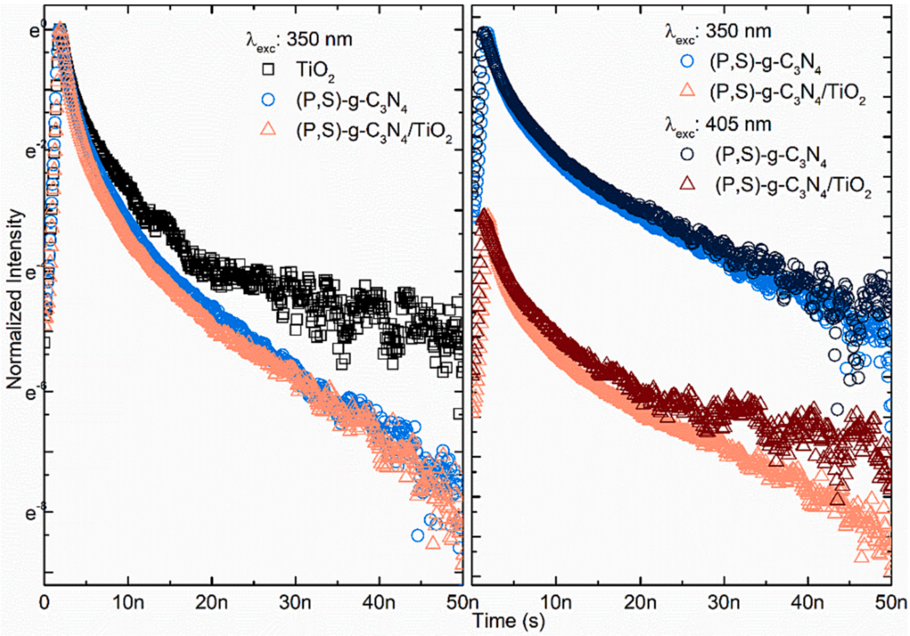

Fig. 8. Luminescence decay curves registered for the TiO_2, (P, S)-g-C_3N_4, and (P, S)-doped g-C_3N_4/TiO_2 (5 %) photocatalysts under two different excitation wavelengths.

Table 2
Decay times were calculated for 2D TiO_2, (P, S)-g-C_3N_4, and (P, S)-g-C_3N_4/TiO_2 (5 %) photocatalysts under two different excitation wavelengths.

Decay times (ns)			
	TiO_2	(P, S)-g-C_3N_4	(P, S)-g-C_3N_4/TiO_2
		λ_{exc}: 350 nm	
τ_1	0.81	0.68	0.6
τ_2	4.49	2.45	2.13
τ_3	207	8.69	7.31
		λ_{exc}: 405 nm	
τ_1	–	0.92	1.25
τ_2	–	2.99	4.61
τ_3	–	10.9	125

6 is proper for the heterojunction formation since the negatively charged surface of (P, S)-g-C_3N_4 could come in contact with positively charged 2D TiO_2 via electrostatic attractions to form the composites; hence, phosphorus and sulfur co-doped carbon nitride are layered upon 2D TiO_2 nanosheet. Besides, during the photodegradation process, based on zeta potential measurements, higher stability of suspension can be noticed at a pH of about 5 and above 7. In the natural environment, pH ranges from 6 to 7. The pKa value of CBZ is 13.9 and ACT is about 9.5. Therefore, CBZ will primarily be present in its protonated form (pH < pKa), while acetaminophen is largely unionized over the neutral range of pH.

Furthermore, the optical properties of the most efficient (P, S)-g-C_3N_4/ 2D TiO_2 (5 % wt) photocatalyst suspension and 2D TiO_2 for comparison were evaluated by means of photon flux measurements. The UVA spectral-average mass extinction coefficient (β) and mass absorption coefficient (κ) were determined for suspensions of both powders, followed by calculation of the scattering coefficient (σ) and albedo (ω) Fig. 10 (a, b) [39]. Based on the obtained values, the local volume rate of photon absorption (LVRPA) was calculated numerically for a cross-section of the reactor, following the six-flux model approach [41] with the scattering probabilities adapted from reported studies of TiO_2, based on the Henyey-Greenstein phase function (details [62]). Finally, integration of the LVRPA values over the analyzed cross-section was performed to obtain the total rate of the photon absorption (TRPA) for a unit of reactor height and was compared with the incident photon flux value.

Obtained data have shown that modification of 2D TiO_2 with 5 % (P, S)-g-C_3N_4 has a very limited effect on the optical properties of the

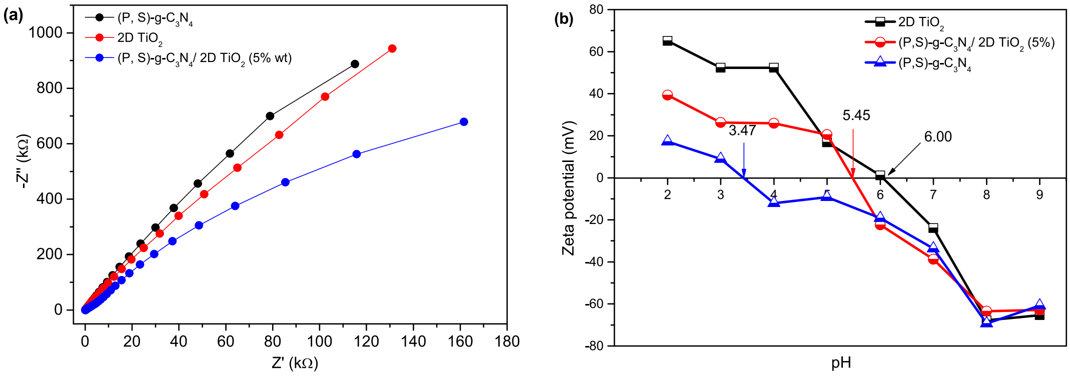

Fig. 9. EIS Nyquist plots for (P, S)-g-C_3N_4, 2D TiO_2 and (P, S)-g-C_3N_4/TiO_2 (5 %) (a), zeta potential determined from the electrophoretic mobility in dependence of the pH, I = $1 \cdot 10^{-2}$ M KCl (b).

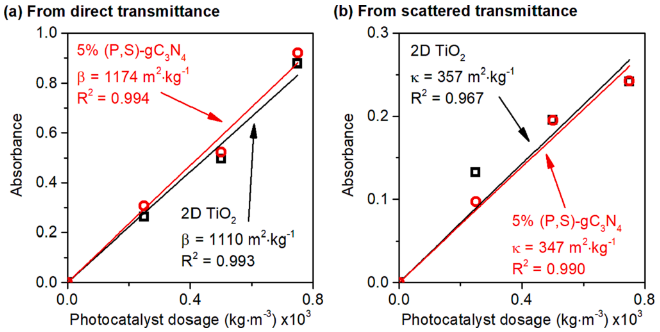

Fig. 10. Dependence of the UVA spectral-average absorbance of the photocatalyst suspension on the photocatalyst dosage, obtained from the transmittance measurements: (a) without including scattered part of the radiation and (b) including radiation scattered through the suspension. Beta and kappa values are slopes of the fitted lines.

suspension. This is followed by almost identical LVRPA distribution inside the reactor, which was plotted for the used concentration (1 g/dm^3) Fig. 11 (a, b). For both materials, the TRPA essentially achieves a quite stable value of 2 W/m for this concentration, with only a slight, linear increase observed with further increase of the photocatalyst dosage Fig. 11 (c). In both cases, approximately 90 % of all UVA photons introduced to the system should be absorbed at 1 g·dm^{-3}.

Following obtained results, it can be assumed that the observed activity increase does not result from the better UVA light absorption of the composite. Furthermore, since (P, S)-g-C$_3$N$_4$ compose only 5 % of the final material, the electronic interactions between both components should be mostly responsible for the observed activity enhancement, which was also evidenced by other techniques.

3.2. *Photocatalytic degradation of carbamazepine (CBZ) and acetaminophen (ACT)*

The photocatalytic activity of prepared photocatalysts was studied in the degradation of carbamazepine and acetaminophen, pharmaceuticals belonging to the group of emerging contaminants, which are not susceptible to biological degradation. As shown in Fig. 12a, doping the graphitic carbon nitride by phosphorus and sulfur increased the photocatalytic activity in the reaction of carbamazepine degradation. The degradation increased from 49 % for g-C$_3$N$_4$ to almost 100 % for (P, S)-g-C$_3$N$_4$ within 120 min of irradiation, while the TOC values presented in Table S1 (Supporting Material) were 14 % and 18 %, respectively. Moreover, the combination of (P, S)-g-C$_3$N$_4$ and 2D TiO$_2$ significantly improved the removal of carbamazepine from the aqueous phase. Furthermore, the observed degradation efficiency of g-C$_3$N$_4$/TiO$_2$ (5 %) was markedly lower compared to all obtained (P, S)-doped g-C$_3$N$_4$/TiO$_2$ composites, confirming the positive effect of (P,S) co-doping of g-C$_3$N$_4$, as presented in Figure S6 in the Supporting Material. For example, the time needed to complete degradation of carbamazepine was 2-times lower for g-C$_3$N$_4$/TiO$_2$ (5 %) than (P, S)- g-C$_3$N$_4$/TiO$_2$ (5 %), and the mineralization efficiency was 42 % and 76 %, respectively. Among the series of (P, S)- g-C$_3$N$_4$/TiO$_2$ photocatalysts, (P, S)-doped g-C$_3$N$_4$/TiO$_2$ (5 %) composite revealed the highest photodegradation efficiency of about 95 % within only 15 min of irradiation. After 30 min of irradiation, complete carbamazepine photodegradation was noticed. The kinetics of reaction for CBZ degradation in the presence of the photocatalysts was studied, and the reactions fit the model of first-order kinetics ($R^2 > 0.97$) (see Fig. 12b).

From kinetics modeling results, it was proved that doping of carbon nitride with phosphorus and sulfur increased the photocatalytic efficiency, and preparation of composites of (P, S)-g-C$_3$N$_4$/TiO$_2$ increased the synergy of reaction, which resulted in complete and fast degradation

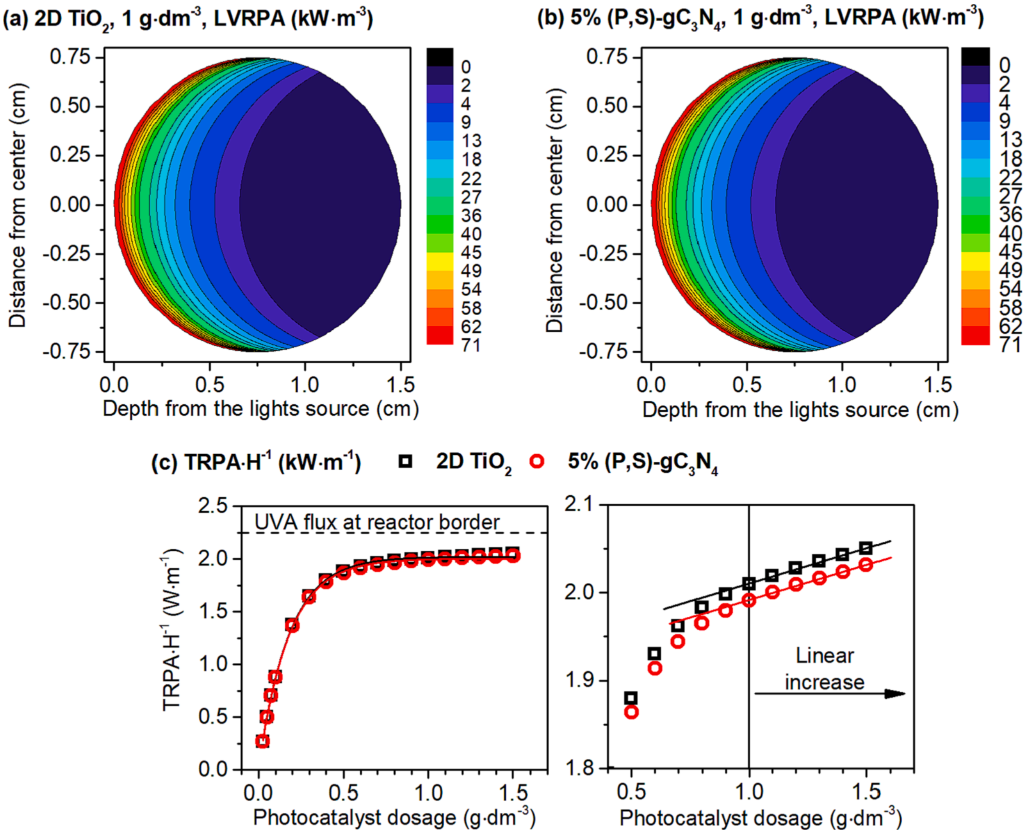

Fig. 11. LVRPA distribution in the cross-section of photoreactor for the control 2D TiO$_2$ (a) and (P, S)-g-C$_3$N$_4$/ 2D TiO$_2$ (5 % wt) (b); integrated LVRPA values for the analyzed cross section as the function of possible photocatalyst-dosage (c).

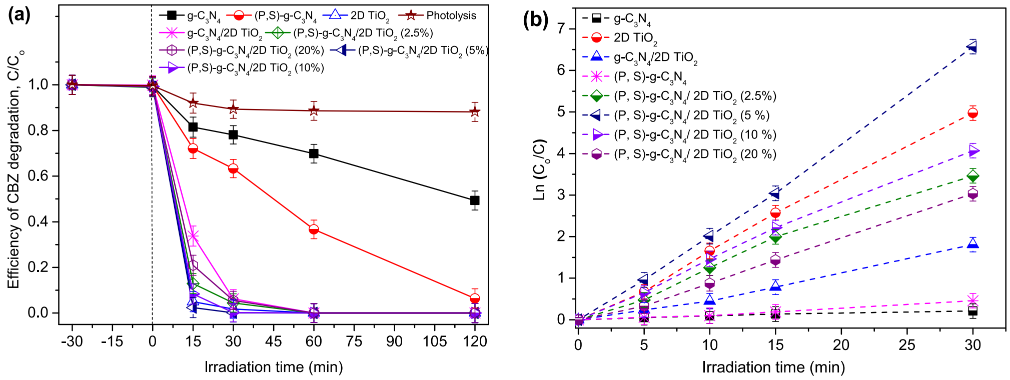

Fig. 12. The efficiency of carbamazepine photodegradation (a), photodegradation kinetics curves for the most active photocatalysts (b). Experimental conditions: C_{CBZ} = 14 mg·dm^{-3}, photocatalyst loading of 1 g· dm^{-3}, water temperature 20 °C, neutral pH, and 120 min of UV–vis light irradiation.

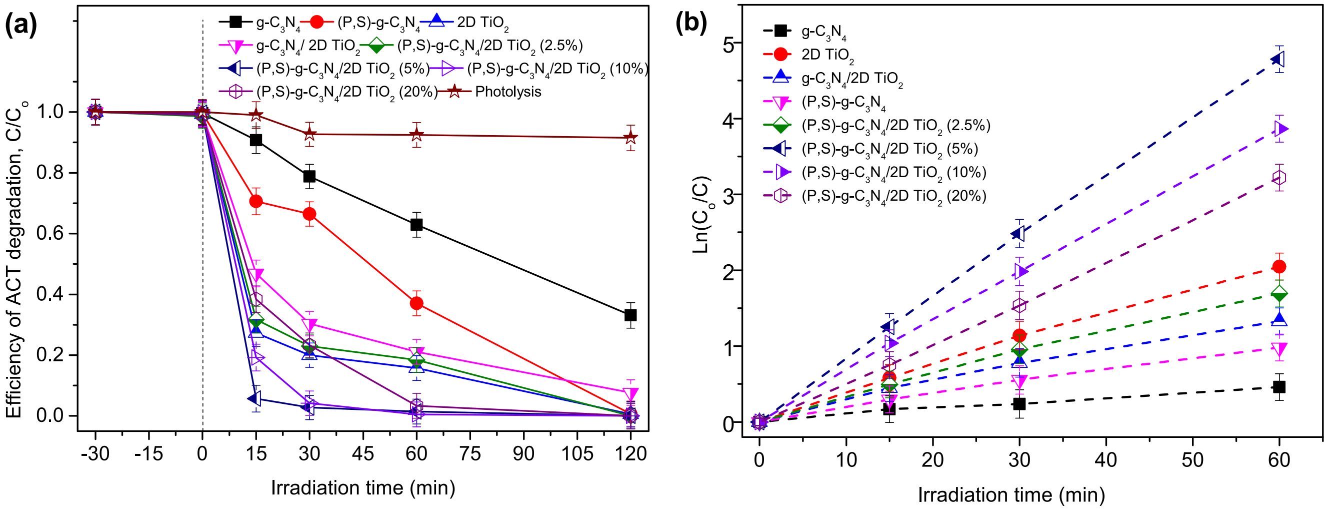

Fig. 13. The efficiency of acetaminophen photodegradation (a), photodegradation kinetics curves for the most active photocatalysts (b). Experimental conditions: C_{ACT} = 20 mg·dm^{-3}, photocatalyst loading of 1 g· dm^{-3}, water temperature 20 °C, neutral pH, and 120 min of UV–vis light irradiation.

of CBZ. Specifically, the lowest rate constant was observed for undoped g-C_3N_4 (see Table S1). The phosphorus and sulfur co-doping of g-C_3N_4 increased the rate constant to 4-fold. For the most active photocatalyst of (P, S)-g-C_3N_4/TiO_2 (5 %), the degradation rate constant was 0.203 min^{-1}, compared to lower degradation of (P, S)-g-C_3N_4/TiO_2 (10 %), (P, S)-g-C_3N_4/TiO_2 (2.5 %), and 2D TiO_2 with a rate constant of 0.161 min^{-1}, 0.133 min$^{-1,}$ and 0.128 min^{-1}, respectively.

Furthermore, it was noticed that acetaminophen is more persistent than carbamazepine, hence degradation time needed to remove this pharmaceutical from the solution completely was 2-times longer (see Fig. 13). The pure 2D TiO_2 possessed a higher rate constant of 0.029 min^{-1} than (P, S)-g-C_3N_4, and the combination of both photocatalysts resulted in increased rate constants and activity (see Table S2 in the Supporting Material). Besides, the acetaminophen degradation tests confirmed the best photocatalytic activity of (P, S)-g-C_3N_4/TiO_2 (5 %) with 99.5 % degradation efficiency, the highest rate constant of 0.074 min^{-1}, and TOC removal of 40 % after 60 min of irradiation.

Among composite materials, the lowest photoactivity was observed for (P, S)-g-C_3N_4/TiO_2 (2.5 %), with 85 % degradation after 60 min of irradiation, rate constant of 0.031 min^{-1}, and TOC removal of 35 % with a synergy index of 0.68 (see in Table S2). The photocatalytic activity was followed by (P, S)-g-C_3N_4/TiO_2 (10 %) and (P, S)-g-C_3N_4/TiO_2 (20 %) with 98.5 % and 97 % of ACT removal, and corresponding synergy indexes of 1.62 for (P, S)- g-C_3N_4/TiO_2 (5 %), 1.41 for (P, S)-g-C_3N_4/TiO_2 (10 %) and 1.18 for (P, S)-g-C_3N_4/TiO_2 (20 %). Below and above the optimum amount of (P, S)- g-C_3N_4 (5 %) combined with 2D TiO_2, the degradation rate constants decreased to 0.064 min^{-1}, 0.054 min^{-1} and 0.031 min^{-1} for (P, S)- g-C_3N_4/TiO_2 (10 %), (P, S)- g-C_3N_4/TiO_2 (20 %), and (P, S)- g-C_3N_4/TiO_2 (2.5 %) composites, respectively. Similarly, the effect of phosphorus and sulfur co-doping into g-C_3N_4 proved to be effective in ACT removal, see Figure S6 in the Supporting Material. The higher degradation efficiency was observed for (P, S)-g-C_3N_4 (63 %) compared to undoped g-C_3N_4 (12 %) after 60 min of irradiation. Furthermore, the photocatalytic activity of (P, S)- g-C_3N_4/TiO_2 (5 %) was compared with TiO_2 P25 as a standard photocatalytic material. The improved photocatalytic activity under UV–vis light was observed for (P, S)- g-C_3N_4/TiO_2 (5 %) composite, as shown in Figure S7 in the Supporting Material.

3.3. Influence of key factors – The effect of water matrice, initial pH, pollutant concentration and photocatalyst dosage

Firstly, the role of different inorganic anions and the pH of the aqueous phase were investigated. Sodium sulfite (Na_2SO_3), sodium sulfate (Na_2SO_4), sodium nitrate ($NaNO_3$), sodium chloride (NaCl), and sodium carbonate (Na_2CO_3) in a concentration of 0.1 mM were used as the source of inorganic anions present in the aqueous systems. The photocatalytic degradation efficiency in the absence of anions was 95 % within 15 min and 100 % within 30 min under UV–vis light irradiation. In the presence of monovalent anions of Cl^- and NO_3^-, the irradiation time needed to achieve above 99 % degradation increased 2-times, as presented in Table S3. The presence of Cl^- and NO_3^- inhibited the CBZ

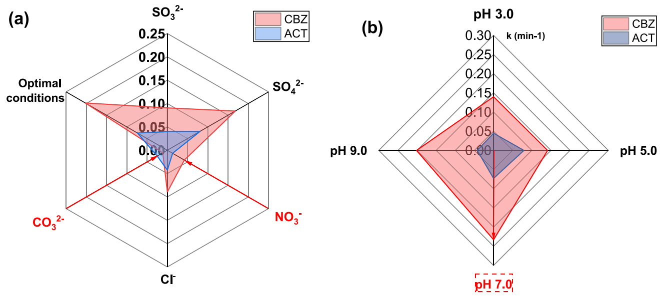

Fig. 14. Radial graphs of water matrice effect (a), pH effect (b) for photodegradation of CBZ and ACT.

degradation process due to the high adsorption affinity of monovalent anions for the composite surface. The rate constants decreased from 0.203 min^{-1} to 0.089 and 0.042 min^{-1}, respectively. Since the photocatalytic process belongs to the radical pathway, this means that the monovalent anions will compete to occupy the active sites in the composite, scavenging thus the hydroxyl and superoxide radicals, which are the main radical species responsible for the degradation of CBZ. Regarding the presence of divalent anions of SO_4^{2-} and CO_3^{2-}, the irradiation time to completely degrade CBZ increased from 30 min to 60 min, whereas the rate constant decreased to 0.168 min^{-1} and 0.112 min^{-1}, see Fig. 14a. Therefore, it can be concluded that the presence of divalent anions in the water phase has a moderate effect on the inhibition of CBZ degradation.

Furthermore, the effect of pH on CBZ degradation in the presence of (P, S)-doped g-C_3N_4/TiO_2 (5 %) composite was studied. The degradation efficiency of CBZ at pH 3, 5, 7, and 9 was found to be 98.5 %, 98.5 %, 100 %, and 100 % within 30 min of irradiation. The corresponding rate constants equaled 0.140 min^{-1}, 0.141 min^{-1}, 0.203 $min^{-1,}$ and 0.201 min^{-1}. Apparently, as presented in Fig. 14b, the neutral and alkaline conditions are more favorable for the degradation of CBZ in the presence of (P, S)-g-C_3N_4/TiO_2 photocatalyst due to higher stability of photocatalyst suspension and attraction between the negatively charged photocatalyst surface ($pH > pH_{IEP}$) and protonated form of carbamazepine.

Regarding ACT degradation, the presence of NO_3^- and CO_3^{2-} inhibited the efficiency of the photocatalytic reaction. The efficiency of ACT degradation equaled 69 % and 68.5 % in 60 min of irradiation compared to 99.5 % degradation in the absence of inorganic anions.

The presence of SO_4^{2-} slightly improved the degradation of ACT with 100 % and a rate constant of 0.080 min^{-1}, whereas the presence of Cl^- slightly decreased the degradation to 91 % with a rate constant of 0.042 min^{-1}. The effect of inorganic anions was compared for 60 min since total degradation was achieved in 120 min for all the samples. Detailed results on the effect of inorganic anions and pH are presented in Table S3. It was observed that the optimal conditions for ACT photodegradation are a pH range between 5 and 7, with a degradation efficiency of almost 100 % in 60 min of irradiation. The rate constants values were 0.079 for pH of 5 and 0.074 min^{-1} for pH of 7.

Furthermore, the effect of ACT and CBZ concentration on the efficiency of the photodegradation process in the presence of (P, S)-doped g-C_3N_4/TiO_2 (5 %) composite was also studied. Primary concentrations of CBZ and ACT were doubled to 28 mg•dm^{-3} and 40 mg•$dm^{-3,}$ respectively. It was found that the increase of CBZ concentration from 14 mg•dm^{-3} to 28 mg•dm^{-3} resulted in the decrease of CBZ degradation efficiency from 100 % to 84 % in 30 min of the degradation process, while the degradation rate decreased from 0.20 min^{-1} to 0.15 min^{-1}. Similarly, for ACT degradation, increasing the pharmaceutical concentration resulted in a decrease of ACT degradation efficiency from 100 % to almost 70 % within 120 min of irradiation, while the degradation rate decreased from 0.07 min^{-1} to 0.03 min^{-1}. However, significant differences are observed comparing the efficiency of TOC removal for the double concentration of the pharmaceuticals in water. The TOC removal efficiency measured as TOC/TOC_0 decreased from 72 % to 7 % for CBZ degradation and from 40 % to 3 % for ACT degradation process, as presented in Table S4 in the Supporting Material. The markedly lower TOC removal efficiency is associated with the formation of by-products.

The effect of photocatalyst amount of 0.5, 1.0, and 2.0 g•dm^{-3} was studied for the removal of CBZ and ACT in their primary concentrations of 14 mg•dm^{-3} and 20 mg•dm^{-3}, respectively. No significant differences were noticed regarding the efficiency of pharmaceuticals degradation. Nevertheless, a slightly higher degradation rate was observed for a photocatalyst amount of.

1.0 g•dm^{-3}, defining it as the optimal photocatalyst dosage, as presented in Table S5 in the Supporting Material. The result regarding the effect of photocatalyst amount was found to be coherent with photon flux measurements.

3.4. Degradation pathway of carbamazepine (CBZ) and acetaminophen (ACT) and mechanism of photodegradation

Since the best photocatalytic activity was revealed for the composite of (P, S)-doped g-C_3N_4/TiO_2 (5 %), the identification of reactive oxygen species responsible for the degradation of CBZ and ACT was performed for the referred composite, as shown in Fig. 15. The results demonstrated that the photocatalytic degradation of CBZ and ACT in the presence of (P, S)-g-C_3N_4/TiO_2 (5 %) was highly inhibited in the presence of *para*-benzoquinone (P-BQ) and isopropanol, which are used as superoxide radicals ($O_2^{•-}$) and hydroxyl radicals (HO$^•$) scavengers. For carbamazepine degradation, in the presence of P-BQ, the efficiency of the reaction

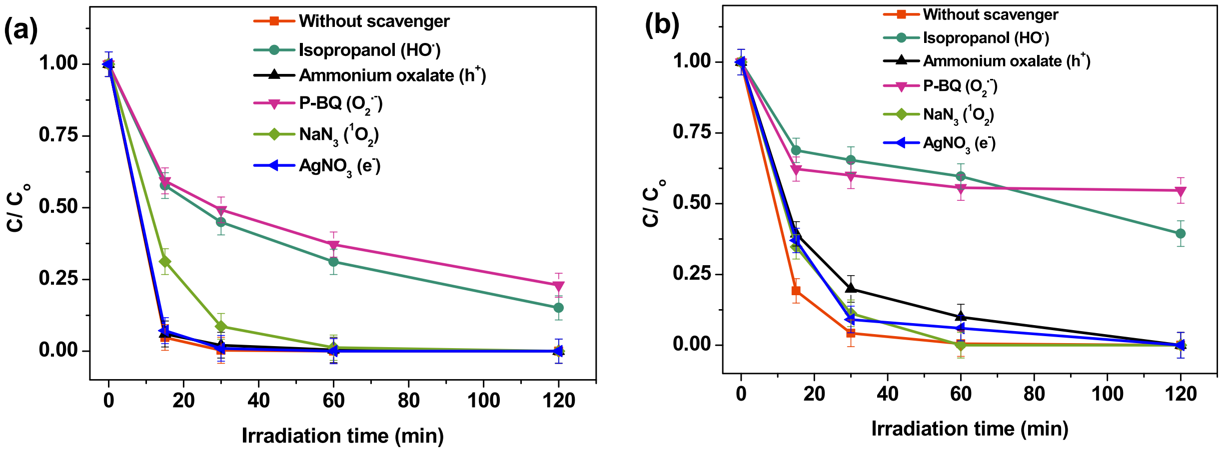

Fig. 15. The degradation efficiency of (P, S)-g-C_3N_4/TiO_2 (5 %) in the presence of scavengers for carbamazepine (a) and acetaminophen (b).

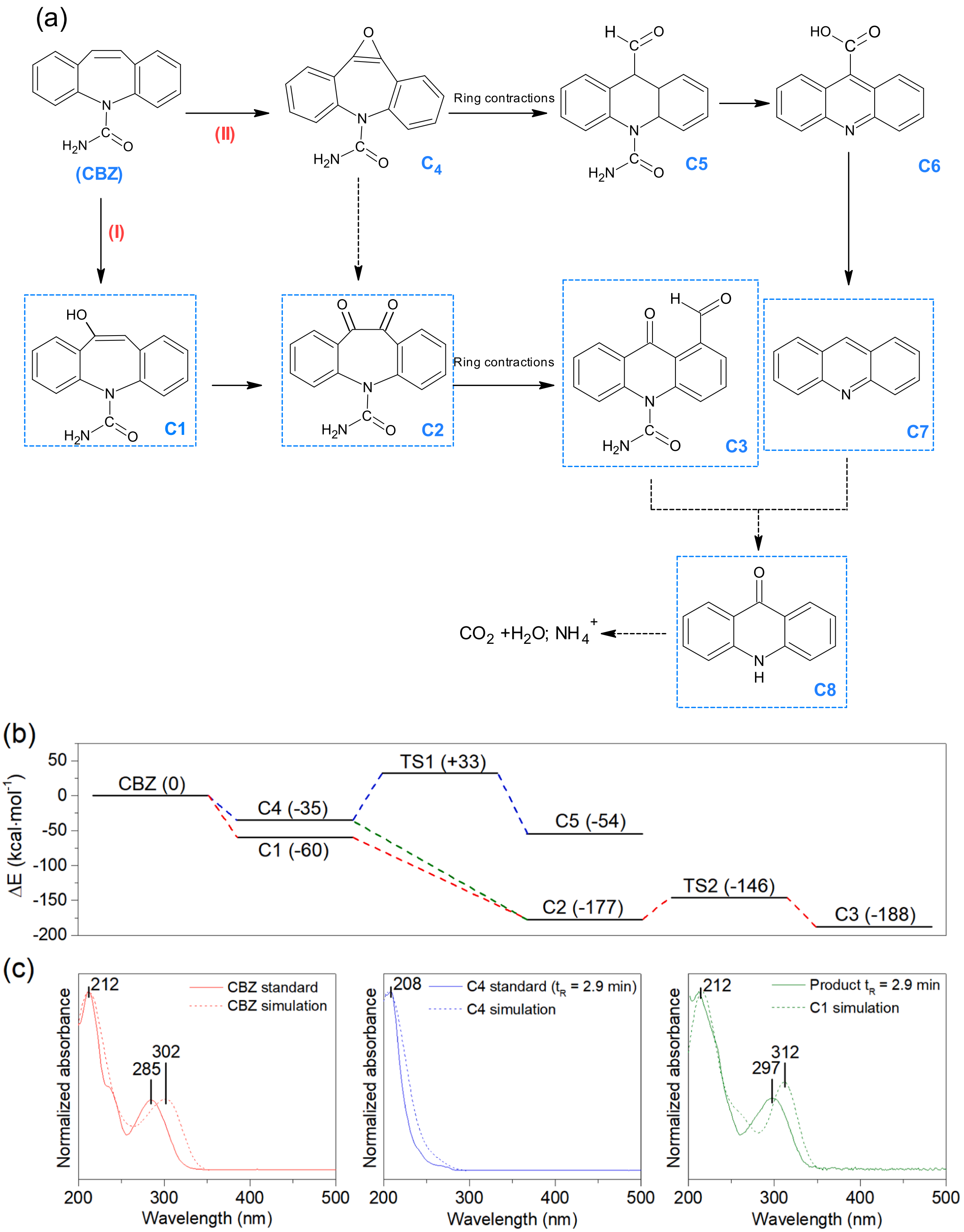

Fig. 16. The proposed mechanism of carbamazepine (a) photocatalytic degradation, together with calculated energy path of the suggested routes (b) and comparison between simulated and observed absorption spectra of the selected compounds (c). Little, consistent shifts of the lower-energy maxima compared in panel (c) result most likely from a bit different environment applied during the HPLC-DAD analysis, which was not simulated in detail.

decreased from 100 % in 30 min to 77 % in 120 min, and the rate constant decreased by 16-fold for the reaction proceeded in the presence of P-BQ and 13-fold in the presence of isopropanol as a $^{\bullet}$OH scavenger. Also, the degradation of ACT decreased from 100 % to 45 % in the presence of P-BQ as an $O_2^{\bullet-}$ scavenger. The introduction of isopropanol inhibited the removal efficiency of ACT to 60.5 % within 120 min of irradiation. The rate constant was 15 times lower than the rate constant for the reaction system in the absence of $O_2^{\bullet-}$ scavenger; meanwhile, the rate constant decreased 10 times in the presence of $^{\bullet}$OH scavenger.

The responsible reactive oxidation species for the degradation of CBZ

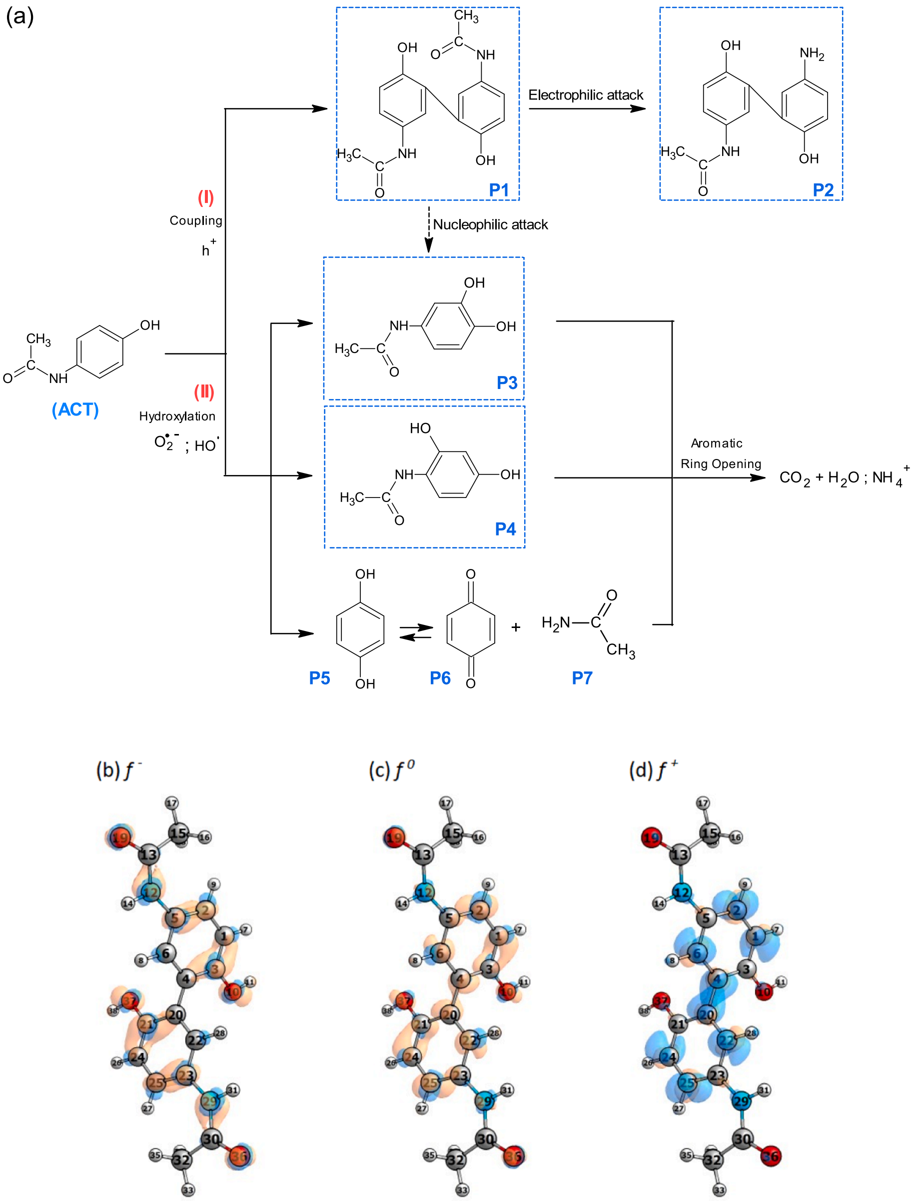

Fig. 17. The proposed mechanism of acetaminophen photocatalytic degradation (a) and calculated maps of Fukui function for compound [P1] (b-d). Carbons, hydrogens, oxygens and nitrogens are grey, white, red and blue spheres. (For interpretation of the references to colour in this figure legend, the reader is referred to the web version of this article.)

and ACT were superoxide radicals ($O_2^{\bullet -}$) and hydroxyl radicals (HO•). Identification of carbamazepine (CBZ) intermediates was performed using LC-MS analysis in combination with additional DFT calculations of the possible by-products formation. Based on the obtained results, the route (I) of CBZ removal was proposed, as presented in Fig. 16a, which especially includes the formation of hydroxy-carbamazepine [C1; *m/z* 271.1] as the initial product. Further degradation of [C1] leads to the formation of dioxo carbamazepine [C2, *m/z* 266.7], which was clearly observed in the MS spectra. These results are in agreement with the performed DFT calculations, which have shown that [C2] is a very stable compound compared to the initial CBZ molecule balanced with the H_2O and O_2 as possible substrates/by-products. Interestingly, this route seems much more probable than alternative path (II), which includes the formation of carbamazepine-10,11-epoxide [C4; *m/z* 271.1], both due to the possible energy effect (shown in Fig. 16b), as well as lack of the [C4] signals observed on the DAD spectra (Fig. 16c).

In this regard, path (I) is proposed as the main route of CBZ degradation in the presence of (P, S)-g-C_3N_4/TiO_2 (5 %) composite. Furthermore, both [C2] and [C4] are also stabilized by the possible ring contraction, forming acridine derivatives as possible by-products. In this case, rearrangement of [C4] to [C5] also seems less probable, as the energy barrier is visibly higher than for the [C2]-[C3]. However, it is noteworthy that this energy barrier [C4]-[C5] can be still overcome by photon absorption ($E_{barrier} = 2.95$ eV), which would fit previous reports showing acridine [C7; *m/z* 179.6] as an important product of CBZ photolysis [63], also observed in this study. Both acridine [C7] and rearranged [C3] might easily form acridone [C8; *m/z* 195.6], which was the final observed by-product. Further oxidation and ring-opening of [C8] may generate short-chain carboxylic acids, and lastly CO_2, H_2O and NH_4^+ may be formed as mineralization products [64].

The degradation pathway of ACT and identified by-products are presented in Fig. 17a. Degradation pathway of ACT follows two main routes, the coupling (I) and hydroxylation/oxidation route (II), with main observed products [P1; *m/z* 300.7], [P3; *m/z* 167.5] and [P4; *m/z* 167.5]. The route (II) ascribed to hydroxylation/oxidation shows transformations typical for the photocatalytic degradation of different

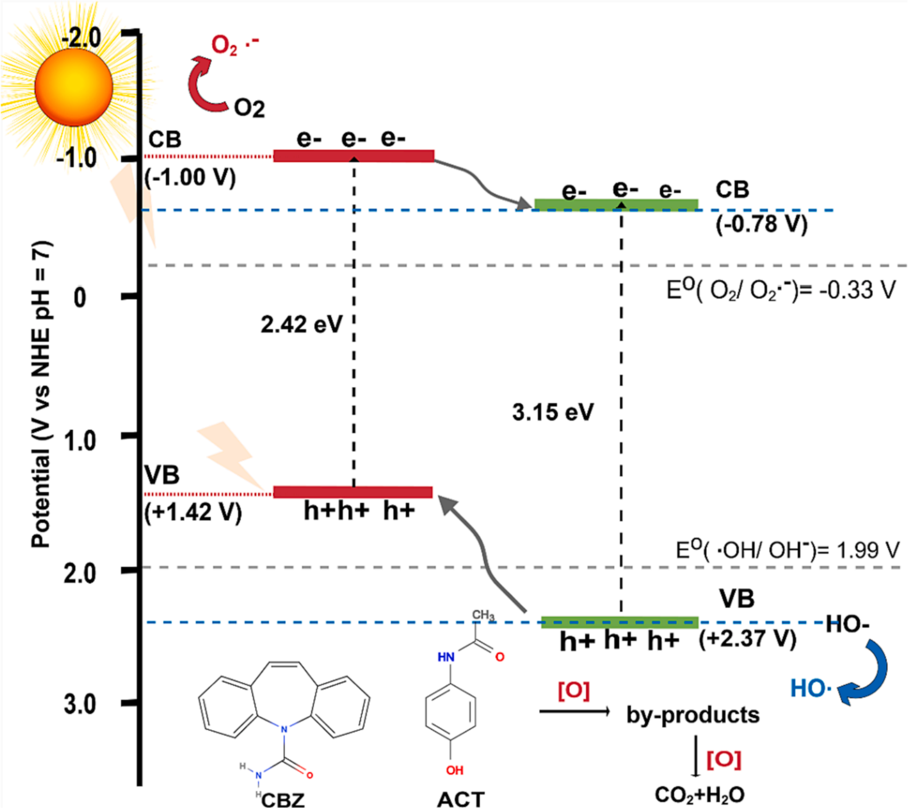

Fig. 18. Schematic illustration of (P,S)-g-C_3N_4/TiO_2 band structure, excitation and photodegradation mechanism of CBZ and ACT under simulated solar light.

aromatic compounds, with –OH substation at the benzene ring. Noteworthy, the elimination of the acetamide [P7; *m/z* 59.04] from ACT molecule also lead to the possible formation of hydroquinone [P5; *m/z* 110.04] and benzoquinone [P6; *m/z* 108.09] as other by-products. All [P3]-[P7] are expected to break into smaller compounds at the further degradation steps and finally generate CO_2, H_2O and NH_4^+, as last-step mineralization products. On the other hand, the formation of the dimer [P1] in route (I) is less typical, and analysis of its possible reactivity is less straightforward. In this regard, additional calculations of the Fukui functions for [P1] were performed to possibly identify reactive sites in its molecule. As shown in Fig. 17b, 17c and 17d majority of active sites are located at the aromatic rings of the dimer, both for the electrophilic attack (f^-), radical attack (f^0) and nucleophilic attack (f^+). These results suggest that further degradation of [P1] might occur similarly for the ACT, but with a larger molecule. However, it is also noteworthy that some differences are noticed between f^- and f^+ maps. Specifically, the electrophilic attack is more probable to occur at the acetamide moiety (atoms N12 and C13 in the Figures), which might lead to the formation of [P2; *m/z* 258.6], as suggested from the MS results. The hydroxyl radicals might especially initiate this transformation since they are electrophilic in nature and were found to be important during the ACT degradation process. On the other hand, the f^+ map clearly shows the preferred site of nucleophilic attack at the dimer-forming bond (C4 and C20 atoms in the Figures), which suggests the hypothetical dissociation of the [P1] back to the smaller molecules is possible as the result of nucleophilic attack. Hypothetically, superoxide radicals might be responsible for such an attack, which might lead to the formation of a product similar to [P3]. This would agree with the observed role of the $\bullet O_2^-$ on the process efficiency, however it should be noted that the reactivity of superoxide radicals is generally slower than other reactive species, so this transformation might not be favored.

Furthermore, based on the Mott-Schottky analysis, the flat band potential of (P, S)-g-C_3N_4/TiO_2 (5 %) heterocomposite was determined. Fig. 18 shows a graphical presentation of the photocatalyst band edges position and charge transfer during excitation with a light greater than its bandgap energy.

The flat band positions of (P, S)-g-C_3N_4 and 2D TiO_2 were calculated to be −1.00 V vs. NHE for (P, S)-g-C_3N_4 and −0.78 V vs. NHE for 2D TiO_2. The valence band edge location was estimated according to a value of the flat band edge position and bandgap energy and amounted to 1.42 V vs. NHE for (P, S)-g-C_3N_4 and 2.37 V vs. NHE for 2D TiO_2. From the photocatalytic mechanism it can be seen that Z-scheme band alignment is formed. Firstly, excited electrons from the valence band (VB) are transferred to the conduction band (CB) and transported onto the photocatalyst surface. The greater photocatalytic activity of (P, S)-g-C_3N_4/TiO_2 nanocomposite compared to 2D TiO_2 and (P, S)-g-C_3N_4 could be attributed to the improved electron transport from (P, S)-g-C_3N_4 to the TiO_2 surface due to the heterojunction formation. Accumulated electrons participate in superoxide anion radicals generation from oxygen as a main reactive oxygen species taking part in the photocatalytic oxidation reaction. Simultaneously, photoinduced holes (h^+) on the TiO_2 nanosheets are transferred to (P, S)-g-C_3N_4 through efficiently formed heterojunction of (P, S)-g-C_3N_4 and TiO_2. In this way, the recombination of e^--h^+ pairs decreases, and separation efficiency increases, which was confirmed by EIS Nyquist plots analysis as well as emissions and decay times measurements. Since the VB of 2D TiO_2 (2.37 eV) is higher than the standard redox potential of E^o ($HO^-/HO^\bullet$) the photoinduced holes can interact with water molecules and produce hydroxyl radicals ($HO^\bullet$).

Finally, the reusability tests were performed for pure 2D TiO_2, (P, S)-g-C_3N_4, and the most active composite of (P, S)-g-C_3N_4/TiO_2 (5 %), as presented in Figure S8. The (P, S)-g-C_3N_4/TiO_2 (5 %) showed better stability than (P, S)-g-C_3N_4 and 2D TiO_2. Regarding pharmaceuticals degradation through three consecutive cycles of selected photocatalysts, it was observed that the less stable photocatalyst was (P, S)-g-C_3N_4 with a decline of photocatalytic degradation by 1.54-fold, but the combination of (P, S)-g-C_3N_4 with 2D TiO_2 generated a more stable photocatalyst. 2D TiO_2 proved to be a more stable photocatalyst with a decline of photocatalytic degradation of 1.18-fold, therefore in the formation of (P, S)-g-C_3N_4/TiO_2 (5 %) contributed to higher stability of heterocomposite.

4. Conclusions

In summary, the novel 2D TiO_2-based hybrid photocatalysts with improved photocatalytic activity were prepared by heterojunction of TiO_2 nanosheets obtained by simple lyophilization method with multi-anion doped g-C_3N_4. The morphological and physicochemical analyses confirmed the formation of Z-scheme heterojunction between (P, S)-g-C_3N_4 and 2D TiO_2, which improved charge carriers separation due to interfacial charge transfer between TiO_2 and (P, S)-doped g-C_3N_4.

The most effective synthesized photocatalyst was composite (P, S)-doped g-C_3N_4/TiO_2 in the optimum loading of 5 % w/w. Phosphorus and sulfur co-doped graphitic carbon nitride contribute to the lower bandgap energy of the formed heterocomposite inhibiting charge carriers recombination. The photoluminescence spectra and carriers lifetime calculations showed better separation of charge carriers in UV light for 2D TiO_2 and under 405 nm excitation (absorption maximum of (P, S)-g-C_3N_4 and sideband of (P, S)-g-C_3N_4/TiO_2 for the composite material. The responsible species for the degradation of pharmaceuticals were superoxide ($O_2^{\bullet -}$) and hydroxyl radicals ($HO^{\bullet}$), which contributed to the complete photodegradation of studied pharmaceuticals. For carbamazepine, about 100 % degradation was achieved within 30 min of photodegradation, whereas for acetaminophen, complete removal was observed in 60 min of irradiation. Moreover, the mineralization efficiency measured as TOC values was 76 % for carbamazepine and 40 % for acetaminophen.

A possible mechanism for carbamazepine and acetaminophen photodegradation was proposed over (P, S)-doped g-C_3N_4/ 2D TiO_2 (5 %) photocatalyst, showing dual advantages of increased light-harvesting capacity and efficient charge carriers separation due to heterojunction (P, S)-doped g-C_3N_4 and 2D TiO_2. The optimal (5 %) (P, S)-doped g-C_3N_4/ 2D TiO_2 (5 %) photocatalyst was stable after subsequent cycles of carbamazepine and acetaminophen degradation.

CRediT authorship contribution statement

Elvana Cako: - there is missing of credit authorship of two authors, please add: Grzegorz Trykowski - Formal analysis, Paweł Głuchowski - Formal analysis, Marcin Pisarek - Formal analysis, Data curation, Formal analysis, Investigation, Visualization, Writing - original draft. **Szymon Dudziak:** Data curation, Formal analysis, Investigation, Software, Visualization. **Agnieszka Fiszka Borzyszkowska:** Formal analysis. **Paweł Głuchowski:** Formal analysis. **Grzegorz Trykowski:** Formal analysis. **Marcin Pisarek:** Formal analysis. **Karol Sikora:** Formal analysis. **Anna Zielińska-Jurek:** Conceptualization, Formal analysis, Supervision, Project administration, Funding acquisition, Methodology, Resources, Writing - original draft, Writing - review & editing.

Declaration of Competing Interest

The authors declare that they have no known competing financial interests or personal relationships that could have appeared to influence the work reported in this paper.

Data availability

Data will be made available on request.

Acknowledgment

The research was financially supported by the Polish National Science Centre (grant no. NCN 2021/43/B/ST5/02983). Financial support from Gdańsk University of Technology under the Oxygenium program supporting open access publications is acknowledged.

Appendix A. Supplementary material

Supplementary data to this article can be found online at https://doi.org/10.1016/j.seppur.2023.123320.

References

[1] K.M. Blum, S.H. Norström, O. Golovko, R. Grabic, J.D. Järhult, O. Koba, H. Söderström Lindström, Removal of 30 active pharmaceutical ingredients in surface water under long-term artificial UV irradiation, Chemosphere 176 (2017) 175–182, https://doi.org/10.1016/j.chemosphere.2017.02.063.

[2] R. Singh, I.S. Thakur, Cancer treatment drugs and endocrine-disrupting chemicals release and fate in hospital wastewater, BV (2020), https://doi.org/10.1016/b978-0-12-819722-6.00007-9.

[3] S. Obimakinde, O. Fatoki, B. Opeolu, O. Olatunji, Veterinary pharmaceuticals in aqueous systems and associated effects: an update, Environ. Sci. Pollut. Res. 24 (4) (2017) 3274–3297.

[4] W.J. Sim, J.W. Lee, E.S. Lee, S.K. Shin, S.R. Hwang, J.E. Oh, Occurrence and distribution of pharmaceuticals in wastewater from households, livestock farms, hospitals and pharmaceutical manufactures, Chemosphere 82 (2011) 179–186, https://doi.org/10.1016/j.chemosphere.2010.10.026.

[5] N.H. Tran, K.Y.H. Gin, Occurrence and removal of pharmaceuticals, hormones, personal care products, and endocrine disrupters in a full-scale water reclamation plant, Sci. Total Environ. 599–600 (2017) 1503–1516, https://doi.org/10.1016/j.scitotenv.2017.05.097.

[6] B. Petrie, D. Camacho-Muñoz, Analysis, fate and toxicity of chiral non-steroidal anti-inflammatory drugs in wastewaters and the environment: a review, Environ. Chem. Lett. 19 (2021) 43–75, https://doi.org/10.1007/s10311-020-01065-y.

[7] H. Jaeschke, F.J. Murray, A.D. Monnot, D. Jacobson-Kram, S.M. Cohen, J. F. Hardisty, E. Atillasoy, A. Hermanowski-Vosatka, E. Kuffner, D. Wikoff, G. A. Chappell, S.B. Bandara, M. Deore, S.K. Pitchaiyan, G. Eichenbaum, Assessment of the biochemical pathways for acetaminophen toxicity: Implications for its carcinogenic hazard potential, Regul. Toxicol. Pharmacol. 120 (2021), 104859, https://doi.org/10.1016/j.yrtph.2020.104859.

[8] S. Dudziak, Z. Bielan, P. Kubica, A. Zielińska-Jurek, Optimization of carbamazepine photodegradation on defective TiO2-based magnetic photocatalyst, J. Environ. Chem. Eng. 9 (2021), 105782, https://doi.org/10.1016/j.jece.2021.105782.

[9] S. Sharma, R.K. Yadav, A.P. Singh, Presence of medicinal materials in drinking water: A review, Mater. Today Proc. (2021), https://doi.org/10.1016/j.matpr.2021.10.336.

[10] D. Mousel, D. Bastian, J. Firk, L. Palmowski, J. Pinnekamp, Removal of pharmaceuticals from wastewater of health care facilities, Sci. Total Environ. 751 (2021), 141310, https://doi.org/10.1016/j.scitotenv.2020.141310.

[11] A. Jos, G. Repetto, J.C. Rios, M.J. Hazen, M.L. Molero, A. del Peso, M. Salguero, P. Fernandez-Freire, J.M. Perez-Martın, A. Camean, Ecotoxicological evaluation of carbamazepine using six different model systems with eighteen endpoints, Toxicol. In Vitro 17 (2003) 525–532, https://doi.org/10.1016/S0887-2333(03)00119-X.

[12] V. Roveri, L. Lopes Guimarães, W. Toma, A.T. Correia, Occurrence, ecological risk assessment and prioritization of pharmaceuticals and abuse drugs in estuarine waters along the São Paulo coast, Brazil, Environ. Sci. Pollut. Res. 29 (2022) 89712–89726, https://doi.org/10.1007/s11356-022-21945-w.

[13] Y.F. Rao, L. Qu, H. Yang, W. Chu, Degradation of carbamazepine by Fe(II)-activated persulfate process, J. Hazard. Mater. 268 (2014) 23–32, https://doi.org/10.1016/j.jhazmat.2014.01.010.

[14] M. Soufan, M. Deborde, A. Delmont, B. Legube, Aqueous chlorination of carbamazepine: Kinetic study and transformation product identification, Water Res. 47 (2013) 5076–5087, https://doi.org/10.1016/j.watres.2013.05.0.

[15] S. Zhou, Y. Xia, T. Li, T. Yao, Z. Shi, S. Zhu, N. Gao, Degradation of carbamazepine by UV/chlorine advanced oxidation process and formation of disinfection by-products, Environ. Sci. Pollut. Res. 23 (2016) 16448–16455, https://doi.org/10.1007/s11356-016-6823-x.

[16] A.O. Oluwole, E.O. Omotola, O.S. Olatunji, Pharmaceuticals and personal care products in water and wastewater: a review of treatment processes and use of photocatalyst immobilized on functionalized carbon in AOP degradation, BMC Chemistry 14 (62) (2020) 1–29, https://doi.org/10.1186/s13065-020-00714-1.

[17] M.D.G. de Luna, R.M. Briones, C.-C. Su, M.-C. Lu, Kinetics of acetaminophen degradation by Fenton oxidation in a fluidized-bed reactor, Chemosphere 90 (4) (2013) 1444–1448.

[18] C.-M. Dai, X.-F. Zhou, Y.-L. Zhang, Y.-P. Duan, Z.-M. Qiang, T.C. Zhang, Comparative study of the degradation of carbamazepine in water by advanced oxidation processes, Environ. Technol. 33 (2012) 1101–1109, https://doi.org/10.1080/09593330.2011.610359.

[19] M. Xu, C. Wu, Y. Zhou, Advancements in the Fenton process for wastewater treatment, in Advanced Oxidation Processes - Applications, Trends, and Prospects, in: C. Bustillo-Lecompte (Ed.), Advanced Oxidation Processes - Applications, Trends, and Prospects, IntechOpen, 2020.

[20] K.M.S. Hansen, A. Spiliotopoulou, R.K. Chhetri, M.E. Casas, K. Bester, H. R. Andersen, Ozonation for source treatment of pharmaceuticals in hospital

wastewater – Ozone lifetime and required ozone dose, Chem. Eng. J. 290 (2016) 507–514, https://doi.org/10.1016/j.cej.2016.01.027.

[21] J. Völker, M. Stapf, U. Miehe, M. Wagner, Systematic review of toxicity removal by advanced wastewater treatment technologies via ozonation and activated carbon, Environ. Sci. Technol. 53 (2019) 7215–7233, https://doi.org/10.1021/acs.est.9b00570.

[22] G. Iervolino, I. Zammit, V. Vaiano, L. Rizzo, Limitations and prospects for wastewater treatment by UV and visible-light-active heterogeneous photocatalysis: A critical review, Top. Curr. Chem. 378 (2020) 1–7, https://doi.org/10.1007/s41061-019-0272-1.

[23] H. Dong, G. Zeng, L. Tang, C. Fan, C. Zhang, X. He, Y. He, An overview on limitations of TiO_2-based particles for photocatalytic degradation of organic pollutants and the corresponding countermeasures, Water Res. 79 (2015) 128–146, https://doi.org/10.1016/j.watres.2015.04.038.

[24] S. Dudziak, M. Kowalkińska, J. Karczewski, M. Pisarek, K. Siuzdak, A. Kubiak, K. Siwińska-Ciesielczyk, A. Zielińska-Jurek, Solvothermal growth of 0 0 1 exposed anatase nanosheets and their ability to mineralize organic pollutants. The effect of alcohol type and content on the nucleation and growth of TiO2 nanostructures, Appl. Surf. Sci. 565 (2021), 150360, https://doi.org/10.1016/j.apsusc.2021.150360.

[25] I. Malinowska, P. Kubica, P. Madajski, A. Ostrowski, C. Gómez, L. Polo, W. Carvera, A. Bednarski, Zielińska-Jurek, Synthesis, characterization and application of 2D/2D TiO_2-GO-$ZnFe_2O_4$ obtained by the fluorine-free lyophilization method for solar light-driven photocatalytic degradation of ibuprofen, Environ. Sci. Pollut. Res. (2022), https://doi.org/10.1007/s11356-022-24587-0.

[26] M.S.A. Hussien, I.S. Yahia, Hybrid multifunctional core/shell g-C_3N_4@TiO_2 heterojunction nano-catalytic for photodegradation of organic dye and pharmaceutical compounds, Environ. Sci. Pollut. Res. (2021) 29665–29680, https://doi.org/10.1007/s11356-021-12680-9.

[27] J. Cao, W. Nie, L. Huang, Y. Ding, K. Lv, H. Tang, Photocatalytic activation of sulfite by nitrogen vacancy modified graphitic carbon nitride for efficient degradation of carbamazepine, Appl. Catal. B Environ. 241 (2019) 18–27, https://doi.org/10.1016/j.apcatb.2018.09.007.

[28] C. Zhao, Z. Liao, W. Liu, F. Liu, J. Ye, J. Liang, Y. Li, Carbon quantum dots modified tubular g-C_3N_4 with enhanced photocatalytic activity for carbamazepine elimination: Mechanisms, degradation pathway and DFT calculation, J. Hazard. Mater. 381 (2020), 120957, https://doi.org/10.1016/j.jhazmat.2019.120957.

[29] S. Moradi, A.A. Isari, F. Hayati, R. Rezaei Kalantary, B. Kakavandi, Co-implanting of TiO_2 and liquid-phase-delaminated g-C_3N_4 on multi-functional graphene nanobridges for enhancing photocatalytic degradation of acetaminophen, Chem. Eng. J. 414 (2021), 128618, https://doi.org/10.1016/j.cej.2021.128618.

[30] D.E. Lee, S. Moru, W.K. Jo, S. Tonda, Porous g-C_3N_4-encapsulated TiO_2 hollow sphere as a high-performance Z-scheme hybrid for solar-induced photocatalytic abatement of environmentally toxic pharmaceuticals, J. Mater. Sci. Technol. 82 (2021) 21–32, https://doi.org/10.1016/j.jmst.2020.10.084.

[31] D. Zhou, Z. Chen, Q. Yang, C. Shen, G. Tang, S. Zhao, J. Zhang, D. Chen, Q. Wei, X. Dong, Facile Construction of g-C_3N_4 Nanosheets/TiO_2 Nanotube Arrays as Z-Scheme Photocatalyst with Enhanced Visible-Light Performance, ChemCatChem 8 (2016) 3064–3073, https://doi.org/10.1002/cctc.201600828.

[32] X. Chen, X. Li, J. Yang, Q. Sun, Y. Yang, X. Wu, Multiphase TiO_2 surface coating g-C_3N_4 formed a sea urchin like structure with interface effects and improved visible-light photocatalytic performance for the degradation of ibuprofen, Int. J. Hydrogen Energy. 43 (2018) 13284–13293, https://doi.org/10.1016/j.ijhydene.2018.05.111.

[33] Y. Lin, Q. Wang, M. Ma, P. Li, V. Maheskumar, Z. Jiang, R. Zhang, Enhanced optical absorption and photocatalytic water splitting of g-C3N4/TiO2 heterostructure through C&B codoping: A hybrid DFT study, Int. J. Hydrogen Energy. 46 (2021) 9417–9432, https://doi.org/10.1016/j.ijhydene.2020.12.114.

[34] K. Sridharan, E. Jang, T.J. Park, Novel visible light active graphitic C_3N_4-TiO_2 composite photocatalyst: Synergistic synthesis, growth and photocatalytic treatment of hazardous pollutants, Appl. Catal. B Environ. 142–143 (2013) 718–728, https://doi.org/10.1016/j.apcatb.2013.05.077.

[35] J. Huang, D. Li, R. Li, P. Chen, Q. Zhang, H. Liu, W. Lv, G. Liu, Y. Feng, One-step synthesis of phosphorus/oxygen co-doped g-C_3N_4/anatase TiO_2 Z-scheme photocatalyst for significantly enhanced visible-light photocatalysis degradation of enrofloxacin, J. Hazard. Mater. 386 (2020), 121634, https://doi.org/10.1016/j.jhazmat.2019.121634.

[36] W. Ouyang, Y. Ji, S. Tan, Q. Tian, Z. Tong, Visible-light-response g-C_3N_4@N, S-Ti_O2 nanocomposites for superior photocatalysis and photoelectrochemical performance, J. Alloys Compd. 866 (2021), 158964, https://doi.org/10.1016/j.jallcom.2021.158964.

[37] N.D. Shcherban, S.M. Filonenko, M.L. Ovcharov, A.M. Mishura, M.A. Skoryk, A. Aho, D.Y. Murzin, Simple method for preparing of sulfur–doped graphitic carbon nitride with superior activity in CO_2 photoreduction, ChemistrySelect 1 (2016) 4987–4993, https://doi.org/10.1002/slct.201601283.

[38] S. Guo, Z. Deng, M. Li, B. Jiang, C. Tian, Q. Pan, H. Fu, Phosphorus-doped carbon nitride tubes with a layered micro-nanostructure for enhanced visible-light photocatalytic hydrogen evolution, Angew. Chemie. 128 (2016) 1862–1866, https://doi.org/10.1002/ange.201508505.

[39] M.I. Cabrera, O.M. Alfano, A.E. Cassano, Absorption and scattering coefficients of titanium dioxide participate suspensions in water, J. Phys. Chem. 100 (1996) 20043–20050, https://doi.org/10.1021/jp962095q.

[40] G. Li Puma, A. Brucato, Dimensionless analysis of slurry photocatalytic reactors using two-flux and six-flux radiation absorption–scattering models, Cat. Today 122 122 (1-2) (2007) 78–90.

[41] R. Acosta-Herazo, J. Monterroza-Romero, M.Á. Mueses, F. Machuca-Martínez, G. Li Puma, Coupling the Six Flux Absorption-Scattering Model to the Henyey-Greenstein scattering phase function: Evaluation and optimization of radiation absorption in solar heterogeneous photoreactors, Chem. Eng. J. 302 (2016) 86–96, https://doi.org/10.1016/j.cej.2016.04.127.

[42] F. Nesse, Software update: The ORCA program system – Version 5.0, Wiley Interdiscip. Rev. Comput. Mol. Sci. 12 (2022) 1606, 10.1002/wcms.1606.

[43] A. D. Becke, Density-functional thermochemistry. III. The role of exact exchange, J. Chem. Phys. 98 (1993) 5648, 10.1063/1.464913.

[44] X. Du, X. Bai, L. Xu, L. Yang, P. Jin, Visible-light activation of persulfate by TiO_2/g-C_3N_4 photocatalyst toward efficient degradation of micropollutants, Chem. Eng. J. 384 (2020), https://doi.org/10.1016/j.cej.2019.123245.

[45] R. Fagan, D.E. McCormack, S.J. Hinder, S.C. Pillai, Photocatalytic properties of g-C_3N_4-TiO_2 heterojunctions under UV and visible light conditions, Materials (Basel). 9 (2016), https://doi.org/10.3390/ma9040286.

[46] X. Han, Q. Kuang, M. Jin, Z. Xie, L. Zheng, Synthesis of titania nanosheets with a high percentage of exposed (001) facets and related photocatalytic properties, J. Am. Chem. Soc. 131 (2009) 3152–3153, https://doi.org/10.1021/ja8092373.

[47] M. Zarattini, C. Dun, L.H. Isherwood, A. Felten, J. Filippi, M.P. Gordon, L. Zhang, O. Kassem, X. Song, W. Zhang, R. Ionescu, J.A. Wittkopf, A. Baidak, H. Holder, C. Santoro, A. Lavacchi, J.J. Urban, C. Casiraghi, Synthesis of 2D anatase TiO_2 with highly reactive facets by fluorine-free topochemical conversion of 1T-TiS2 nanosheets, J. Mater. Chem. A. 10 (26) (2022) 13884–13894.

[48] S. Panneri, P. Ganguly, B.N. Nair, A.A.P. Mohamed, K.G.K. Warrier, U.N. S. Hareesh, Role of precursors on the photophysical properties of carbon nitride and its application for antibiotic degradation, Environ. Sci. Pollut. Res. 24 (2017) 8609–8618, https://doi.org/10.1007/s11356-017-8538-z.

[49] B. Ma, N. Yu, S. Xin, Y. Xin, C. Zhang, X. Ma, M. Gao, Photoelectrocatalytic degradation of p-chloronitrobenzene by g-C_3N_4/TiO_2 nanotube arrays photoelectrodes under visible light irradiation, Chemosphere 267 (2021), 129242, https://doi.org/10.1016/j.chemosphere.2020.129242.

[50] K. Wang, J. Fu, Y. Zheng, Insights into photocatalytic CO_2 reduction on C_3N_4: Strategy of simultaneous B, K co-doping and enhancement by N vacancies, Appl. Catal. B Environ. 254 (2019) 270–282, https://doi.org/10.1016/j.apcatb.2019.05.002.

[51] Y. Zhang, T. Mori, J. Ye, M. Antonietti, Phosphorus-doped carbon nitride solid: Enhanced electrical conductivity and photocurrent generation, J. Am. Chem. Soc. 132 (2010) 6294–6295, https://doi.org/10.1021/ja101749y.

[52] J. Hong, X. Xia, Y. Wang, R. Xu, Mesoporous carbon nitride with in situ sulfur doping for enhanced photocatalytic hydrogen evolution from water under visible light, J. Mater. Chem. 22 (2012) 15006–15012, https://doi.org/10.1039/c2jm32053c.

[53] G. Liu, P. Niu, C. Sun, S.C. Smith, Z. Chen, G.Q. Lu, H.M. Cheng, Unique electronic structure induced high photoreactivity of sulfur-doped graphitic C_3N_4, J. Am. Chem. Soc. 132 (2010) 11642–11648, https://doi.org/10.1021/ja103798k.

[54] H.Y. Hafeez, S.K. Lakhera, S. Bellamkonda, G.R. Rao, M.V. Shankar, D. W. Bahnemann, B. Neppolian, Construction of ternary hybrid layered reduced graphene oxide supported g-C_3N_4-TiO_2 nanocomposite and its photocatalytic hydrogen production activity, Int. J. Hydrogen Energy. 43 (2018) 3892–3904, https://doi.org/10.1016/j.ijhydene.2017.09.048.

[55] X. Feng, P. Wang, J. Hou, J. Qian, Y. Ao, C. Wang, Significantly enhanced visible light photocatalytic efficiency of phosphorus doped TiO_2 with surface oxygen vacancies for ciprofloxacin degradation: Synergistic effect and intermediates analysis, J. Hazard. Mater. 351 (2018) 196–205, https://doi.org/10.1016/j.jhazmat.2018.03.013.

[56] C. Yang, S. Shang, X. yan Li, Fabrication of sulfur-doped TiO_2 nanotube array as a conductive interlayer of PbO_2 anode for efficient electrochemical oxidation of organic pollutants, Sep. Purif. Technol. 258 (2021) 118035. 10.1016/j.seppur.2020.118035.

[57] J. Jiang, L. Ou-Yang, L. Zhu, A. Zheng, J. Zou, X. Yi, H. Tang, Dependence of electronic structure of g-C3N4 on the layer number of its nanosheets: A study by Raman spectroscopy coupled with first-principles calculations, Carbon N. Y. 80 (2014) 213–221, https://doi.org/10.1016/J.CARBON.2014.08.059.

[58] M.M. Khan, S.A. Ansari, D. Pradhan, M.O. Ansari, D.H. Han, J. Lee, M.H. Cho, Band gap engineered TiO_2 nanoparticles for visible light induced photoelectrochemical and photocatalytic studies, J. Mater. Chem. A. 2 (2014) 637–644, https://doi.org/10.1039/c3ta14052k.

[59] Q. Guo, Y. Zhang, J. Qiu, G. Dong, Engineering the electronic structure and optical properties of g-C_3N_4 by non-metal ion doping, J. Mater. Chem. C. 4 (2016) 6839–6847, https://doi.org/10.1039/C6TC01831A.

[60] Y. Yamada, Y. Kanemitsu, Determination of electron and hole lifetimes of rutile and anatase TiO_2 single crystals, Appl. Phys. Lett. 101 (2012), https://doi.org/10.1063/1.4754831.

[61] C. Ye, J.-X. Li, Z.-J. Li, X.-B. Li, X.-B. Fan, L.-P. Zhang, B. Chen, C.-H. Tung, L.-Z. Wu, Enhanced driving force and charge separation efficiency of protonated g-C_3N_4 for photocatalytic O_2 evolution, ACS Catal. 5 (2015) 6973–6979, https://doi.org/10.1021/ACSCATAL.5B02185.

[62] R. Acosta-Herazo, M.Á. Mueses, G.L. Puma, F. Machuca-Martínez, Impact of photocatalyst optical properties on the efficiency of solar photocatalytic reactors rationalized by the concepts of initial rate of photon absorption (IRPA)

dimensionless boundary layer of photon absorption and apparent optical thickness, Chem. Eng. J. 356 (2019) 839–849, https://doi.org/10.1016/j.cej.2018.09.085.

[63] X. Yuan, S. Li, J. Hu, M. Yu, Y. Li, Z. Wang, Experiments and numerical simulation on the degradation processes of carbamazepine and triclosan in surface water: A case study for the Shahe Stream, South China, Sci. Total Environ. 655 (2019) 1125–1138, https://doi.org/10.1016/j.scitotenv.2018.11.290.

[64] F. Pan, H. Ji, P. Du, T. Huang, C. Wang, W. Liu, Insights into catalytic activation of peroxymonosulfate for carbamazepine degradation by MnO_2 nanoparticles in-situ anchored titanate nanotubes: Mechanism, ecotoxicity and DFT study, J. Hazard. Mater. 402 (2021), 123779, https://doi.org/10.1016/j.jhazmat.2020.123779.